

## REPORT DOCUMENTATION PAGE

The public reporting burden for this collection of information is estimated to average 1 hour per response, including the time for reviewing instructions, searching existing data sources, gathering and maintaining the data needed, and completing and reviewing the collection of information. Send comments regarding this burden estimate or any other aspect of this collection of information, including suggestions for reducing the burden, to the Department of Defense, Executive Service Directorate (0704-0188). Respondents should be aware that notwithstanding any other provision of law, no person shall be subject to any penalty for failing to comply with a collection of information if it does not display a currently valid OMB control number.

**PLEASE DO NOT RETURN YOUR FORM TO THE ABOVE ORGANIZATION.**

|  |             |                         |                            |   |   |
|--|-------------|-------------------------|----------------------------|---|---|
| 1. REPORT DATE (DD-MM-YYYY)<br>01-06-2009  |             | 2. REPORT TYPE<br>Final |                            | 3. DATES COVERED (From - To)<br>11/4/2005-3/31/2009 |   |
| 4. TITLE AND SUBTITLE<br>Characterization of Near Wall Surface Chemistry and Fluid Interaction in Hypersonic Boundary Layers   |             |                         |                            | 5a. CONTRACT NUMBER<br>FA9550-05-1-0490             |   |
|  |             |                         |                            | 5b. GRANT NUMBER                                    |   |
|  |             |                         |                            | 5c. PROGRAM ELEMENT NUMBER                          |   |
| 6. AUTHOR(S)<br>Martin, M.P., Marschall, J., Pejakoavic, D. and Duan L.  |             |                         |                            | 5d. PROJECT NUMBER                                  |   |
|  |             |                         |                            | 5e. TASK NUMBER                                     |   |
|  |             |                         |                            | 5f. WORK UNIT NUMBER                                |   |
| 7. PERFORMING ORGANIZATION NAME(S) AND ADDRESS(ES)<br>Princeton University<br>Mechanical and Aerospace Engineering Dept<br>Olden St E Quad<br>Princeton, NJ 08544  |             |                         |                            | 8. PERFORMING ORGANIZATION REPORT NUMBER<br>1506871 |   |
| 9. SPONSORING/MONITORING AGENCY NAME(S) AND ADDRESS(ES)<br>AFOSR<br>4015 Wilson Blvd<br>Arlington VA 22203<br>Dr. Joan Fuller  |             |                         |                            | 10. SPONSOR/MONITOR'S ACRONYM(S)                    |   |
|  |             |                         |                            | 11. SPONSOR/MONITOR'S REPORT NUMBER(S)              |   |
| 12. DISTRIBUTION/AVAILABILITY STATEMENT<br>Distribution A  |             |                         |                            |   |   |
| <b>20090706010</b>   |             |                         |                            |   |   |
| 13. SUPPLEMENTARY NOTES  |             |                         |                            |   |   |
| 14. ABSTRACT<br>We have demonstrated the importance of the O + N surface reaction for catalytic atom recombination in dissociated nitrogen oxygen mixtures. This was accomplished using numerical and experimental studies in a tube side arm reactor, a microwave discharge to generate atomic nitrogen and an NO titration technique to generate different mixtures of O and N atoms.<br>In the first approach, two photon LIF of atomic oxygen and atomic nitrogen were used to show how the relative atom concentration varied with position along the diffusion tube as a function of O/N ratio at the diffusion tube inlet. The experimental and numerical results confirmed and extended earlier experiments.<br>In the second approach, single photon LIF was used together with isotropically labeled titration gases to detect surface produced NO directly at two different positions in the diffusion tube as a function of O/N ratio at the diffusion tube inlet. |             |                         |                            |   |   |
| 15. SUBJECT TERMS<br>titration, NO, gases, detect, positions   |             |                         |                            |   |   |
| 16. SECURITY CLASSIFICATION OF:  |             |                         | 17. LIMITATION OF ABSTRACT | 18. NUMBER OF PAGES                                 | 19a. NAME OF RESPONSIBLE PERSON                           |
| a. REPORT  | b. ABSTRACT | c. THIS PAGE            |                            |   | Pino Martin   |
|  |             |                         |                            |   | 19b. TELEPHONE NUMBER (Include area code)<br>609-258-7318 |

# **Characterization of Near Wall Surface Chemistry and Fluid Interaction in Hypersonic Boundary Layers**

Award Number: FA9550-05-1-0490

Type of Report: Final

Co-PI: Jochen Marschall, SRI International, Molecular Physics Laboratory

Co-PI: M. Pino Martin, Princeton University, MAE Department

Other personnel:

Dušan Pejaković, SRI International

Lian Duan, Princeton University

Period of Performance: 11/4/2005 – 3/31/2009

Prepared for:

Dr. Joan Fuller

Dr. John Schmisser

## INTRODUCTION

This report summarizes the activities performed by Molecular Physics Laboratory personnel under SRI Project P17002 (Subcontract No. 00001131, The Trustees of Princeton University). The Principal Investigator for this project was Dr. Jochen Marschall and the Co-Investigator was Dr. Dušan Pejaković. The period of performance was 11/4/2005 to 3/31/2009.

This SRI subcontract supports a prime contract awarded to Princeton University by the Air Force Office of Scientific Research entitled, "Characterization of Near Wall Surface Chemistry and Fluid Interaction in Hypersonic Boundary Layers", with Prof. Maria P. Martin as the Principal Investigator. The statement of work for the SRI subcontract is:

*SRI will use a high-power microwave discharge flow tube coupled with mass spectroscopic and laser-based diagnostics to investigate heterogeneous processes on heated test specimens as a function of sample temperature, gas pressure, and gas composition. The microwave discharge facility will enable testing in clean, controlled gas environments with high levels of atomic oxygen and atomic nitrogen. Silicon carbide, carbon and other specimens will be tested, in quantities and with specifications to be determined by mutual discussion.*

*SRI will use its expertise in optical, laser-based, and mass spectroscopic techniques to quantify the chemical composition of the test environment, and to monitor changes in reactant and product concentrations as a function of various experimental parameters. Changes in sample mass and morphology will be documented and correlated with gas-phase diagnostics. The experimental results will be used to construct finite-rate surface chemistry models for use in computational fluid dynamics simulations.*

During the course of this study, the decision was made to focus on catalytic processes on silica surfaces in partially dissociated oxygen-nitrogen gas mixtures. This choice was motivated by several factors, including i) many reusable thermal protection systems either have silica-based protective coatings or form silica-rich oxides scales upon oxidation, ii) limited experimental information is currently available in the literature on the products and production channels of O- and N-atom surface recombination, and iii) catalytic processes are the logical starting points for developing and testing finite-rate surface reaction models before extending such models to surface consuming processes.

The following section presents some background on the problem of O and N surface recombination and its importance to aerothermal heating.

The next section describes our initial set of experiments which were aimed at confirming and extending previous room-temperature measurements suggesting the importance of nitric oxide (NO) as surface recombination product in partially dissociated oxygen-nitrogen mixtures. These experiments used a diffusion tube side-arm reactor in conjunction with two-photon laser-induced fluorescence (LIF) detection of atomic oxygen and atomic nitrogen. With modeling support by our Princeton collaborators, Lian Duan and Pino Martin, our experimental results demonstrate that NO formation is as significant a pathway as O<sub>2</sub> and N<sub>2</sub> formation. The results of these studies were presented as a conference paper<sup>1</sup> at the 46<sup>th</sup> AIAA Aerospace Sciences Meeting and Exhibit, January 7-10, 2008 in Reno, NV and later published in the AIAA Journal of Thermophysics and Heat Transfer.<sup>2</sup>

The last section of the report describes our follow-on experiments aimed at detecting the surface production of NO directly at elevated temperatures, using single-photon LIF excitation scans as an NO diagnostic, together with isotopically-enriched <sup>15</sup>N<sup>16</sup>O and <sup>15</sup>N<sup>18</sup>O titration gases to isolate surface-produced NO from all other possible sources. These experiments independently confirm the

surface production of nitric oxide and provide data that can be compared with the predictions of finite-rate surface reaction models.

## BACKGROUND

The heterogeneous recombination of dissociated species on the surface of thermal protection system (TPS) materials is known to contribute to the aerothermal heating of hypersonic reentry vehicles. In the Earth's atmosphere, oxygen and nitrogen atoms are generated in the shock layer ahead of leading edges during hypersonic flight. Modeling O- and N-atom surface-catalyzed recombination is an important part of computational fluid dynamics (CFD) simulations that predict aerothermal heating as a function of flight trajectory.

Traditionally, CFD aerothermal heating computations have treated oxygen and nitrogen recombination as two uncoupled parallel processes,  $O + O \rightarrow O_2$  and  $N + N \rightarrow N_2$  neglecting the possibility of NO formation via  $O + N$  surface reactions. This choice is partly a matter of computational convenience and partly due to the lack of experimental information on the importance of the NO formation pathway. More recent modeling efforts have introduced finite rate kinetic models to better capture the physics of surface catalytic reactions.<sup>3-9</sup> In at least one case, the inclusion of NO surface formation in a finite-rate surface chemistry model seems to improve agreement between aerothermal heating computations and measured flight data.<sup>7</sup> Strong support for NO surface formation is also provided by the *in situ* laser-induced fluorescence (LIF) detection of different NO concentrations in front of different materials tested in a plasma wind tunnel.<sup>10</sup>

Copeland et al.<sup>11</sup> reported an experimental approach for inferring the formation of NO in  $N_2/N/O$  gas mixtures using two-photon LIF detection of N atoms in a room temperature diffusion-tube side-arm reactor. In the side-arm reactor technique, atomic species are generated in a main flow tube and diffuse into the opening of a dead-end side-arm tube where they are lost by gas-phase and surface-mediated recombination reactions, establishing a steady-state decaying atom concentration profile along the length of the side-arm tube. At sufficiently low pressures, heterogeneous atom loss processes dominate over (most) gas-phase reactions, and this atom concentration profile can be related to the catalytic activity of the tube surface.<sup>12-19</sup>

Copeland et al.<sup>11</sup> produced a range  $N_2/N/O$  gas mixtures in the main flow tube by titrating a partially dissociated nitrogen flow with controlled amounts of NO to drive the gas-phase reaction  $N + NO \rightarrow N_2 + O$ . This bimolecular reaction produces one O atom for every NO consumed and is very rapid with a room-temperature rate coefficient<sup>20</sup> of  $3 \times 10^{-11} \text{ cm}^3 \text{ molecule}^{-1} \text{ s}^{-1}$ . They then demonstrated that as O atoms were added to the flowing  $N_2/N$  mixture, the loss of N atoms from the gas-phase within the side-arm tube increased. They interpreted this accelerated N-atom loss as resulting from the same gas phase  $N + NO \rightarrow N_2 + O$  reaction, where the NO source was now N + O surface recombination on the walls of the side-arm tube.

Under the low pressures of their experiment (13 to 65 Pa), the direct production of NO in the gas phase by the three-body  $N + O + M$  reaction was insignificant.<sup>21</sup> Because the  $N + NO \rightarrow N_2 + O$  reaction is so fast and atom concentrations in the side-arm are low, the steady-state gas-phase NO concentrations generated by surface recombination are too small for direct LIF detection, and NO surface formation must be inferred indirectly from observed changes in atom concentrations.

Copeland et al.<sup>11</sup> suggested a further check of their interpretation: if surface NO formation was indeed occurring, O-atom loss from the gas-phase should decrease with the addition of N atoms, since

each reaction event  $N + NO$  regenerates a gas-phase O-atom. However, they did not perform O-atom LIF measurements to confirm this.

### SURFACE PRODUCTION OF NITRIC OXIDE AT ROOM TEMPERATURE: O- AND N-ATOM DETECTION EXPERIMENTS

We have repeated and extended the measurements of Copeland et al.<sup>11</sup> by adding, i) a more powerful discharge source for N-atom production, ii) the capability for sequential N-atom and O-atom LIF diagnostics, and iii) simultaneous concentration measurements at four different side-arm locations.

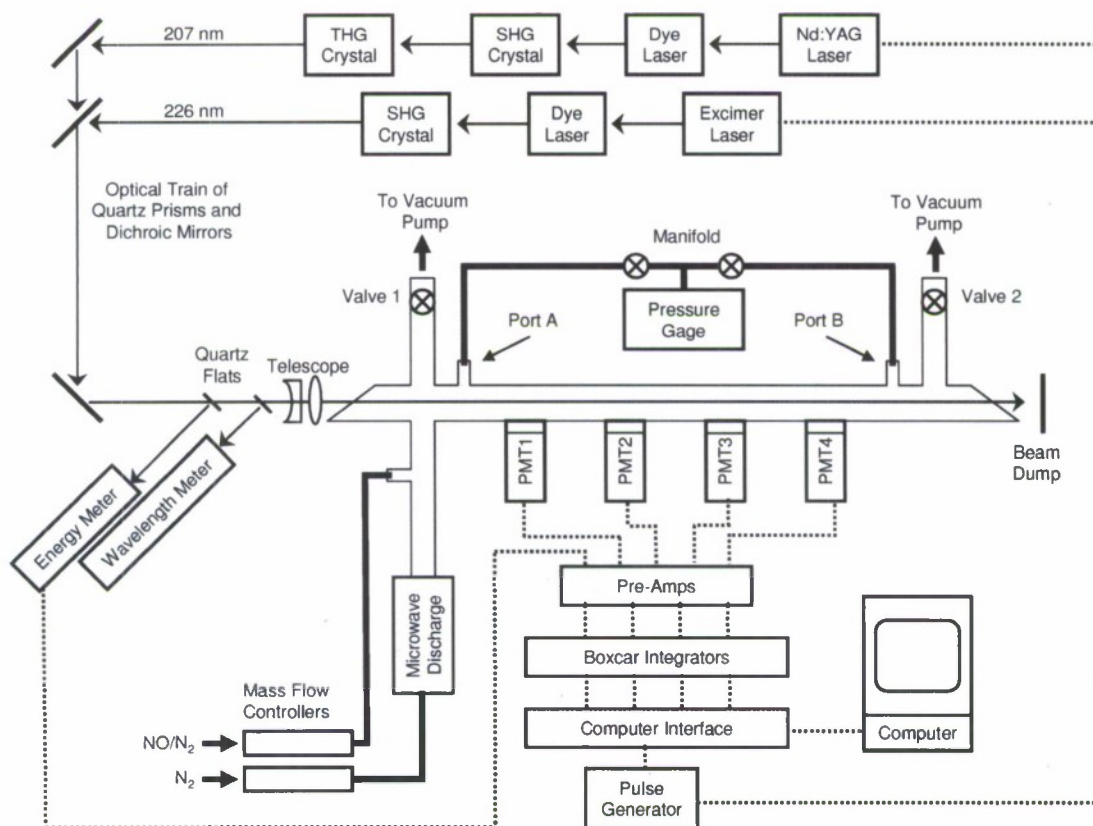


Figure 1. Experimental setup; PMT, SHG, and THG indicate photomultiplier tube, second harmonic generation and third harmonic generation, respectively.

## Experimental Setup

The layout of our experiment is shown in Fig.1. A partially-dissociated nitrogen flow is produced by metering nitrogen through a 6 kW microwave discharge using a 500 standard cubic centimeter per minute (sccm) Tylan mass flow controller. The main tube is made of glass and the side-arm tube is made of GE214 quartz. With valve 1 open and valve 2 closed, the partially-dissociated gas flows down the main arm, past the opening of the dead-end side-arm tube, and into a roots blower vacuum system. In this configuration the side-arm operates as a diffusion tube. The side-arm can be reconfigured as a flow tube by closing valve 1 and opening valve 2. Gas pressures are measured near the opening (port A) and near the end (port B) of the side-arm tube using a 10 Torr capacitance manometer with four digit precision and a reading error less than 1%.

Species detection was accomplished using well-known 2-photon LIF schemes: excitation at 226 nm followed by fluorescence at 845 nm for O-atoms<sup>22,23</sup> and excitation at 207 nm followed by fluorescence at 745 nm for N-atoms.<sup>24</sup> For O-atom LIF, a Lambda-Physik ENG 103 XeCl Excimer laser was used to pump a Lambda-Physik FL 3002 dye laser filled with Coumarin 47 laser dye dissolved in methanol. The resulting tunable blue light near 452 nm was frequency-doubled using a type-B beta barium-borate (BBO) crystal to produce 226 nm radiation. For N-atom LIF, tunable red light near 621 nm was produced by pumping a Quanta-Ray MC1 dye laser filled with Rhodamine 640 dissolved in methanol, with the second harmonic output of a Quanta-Ray DCR-3 Nd:YAG laser. The red light was frequency-tripled to produce 207 nm radiation using type-2 and type-C BBO crystals for frequency doubling and frequency mixing, respectively.

The two ultraviolet laser beams were alternately directed through a quartz Brewster angle window down the centerline of the side-arm tube using different combinations of dichroic mirrors, quartz prisms and collimating optics. A Pellin-Broca prism was used to separate visible from ultraviolet light during the O-atom detection experiments; dichroic mirrors were sufficient to separate visible from UV light during the N-atom experiments. Quartz flats were used to direct small fractions of the laser beam into a Molelectron pyroelectric energy meter and into a Coherent wavemeter, to monitor laser pulse energy and wavelength, respectively. The ultraviolet excitation energy per laser pulse was ~0.5 mJ for O-atom detection and ~0.1 mJ for N-atom detection.

Fluorescence was collected at right angles to the side-arm tube by four red-sensitive Hamamatsu photomultiplier tubes (R636) in gated sockets, fitted with 3-nm bandwidth interference filters centered on 845 nm for O-atom detection and 745 nm for N-atom detection. PMT signals were amplified by a factor of five and averaged over 150 ns wide gates using Stanford Research Systems (SRS) boxcar integrators. Data acquisition and laser firing were synchronized at 10 Hz using a SRS digital delay generator. Automation of the experiment and data collection was performed by a personal computer using LabView software.

The concentration of O atoms in the main gas flow was controlled by adding a 1%NO in N<sub>2</sub> gas mixture to the partially-dissociate nitrogen flow upstream of the side-arm opening. At the N + NO titration endpoint all N atoms are consumed and replaced in the flow by O atoms. The titration endpoint can be detected by the disappearance of the N-atom LIF signal and the leveling off of the O-atom LIF signal.

The experiments were conducted at 298 K, with a 44.4 sccm flow of N<sub>2</sub> into the main arm and the discharge operating at 40% of its maximum capacity (corresponding to ~2.4 kW.) The pressure at port A before any addition of the NO/N<sub>2</sub> gas mixture at the titration port was adjusted to be 60 Pa in both flow tube and diffusion tube experiments, by throttling the flow with the appropriate valve. The maximum gas flow added at the titration port was ~6 sccm, which increased the pressure at port A by

about 1.3 Pa in both flow and diffusion tube modes. In flow tube mode, the pressure difference between ports A and B was approximately 5.3 Pa for all levels of added titration gas flows, resulting in bulk flow velocities ranging from about 3.6 to 3.85 m/s at the different PMT locations. Important experimental dimensions are shown in Fig. 2. The spacing between PMTs is 25.4 cm and the spacing between pressure ports A and B is 120 cm. The inner diameter of the side-arm tube is 2.2 cm.

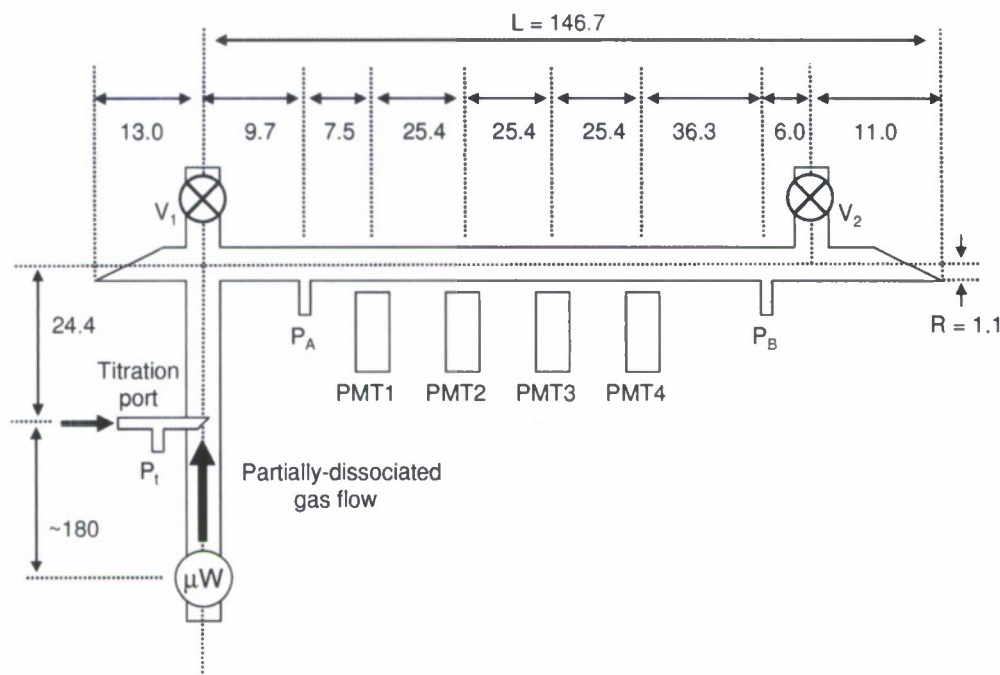
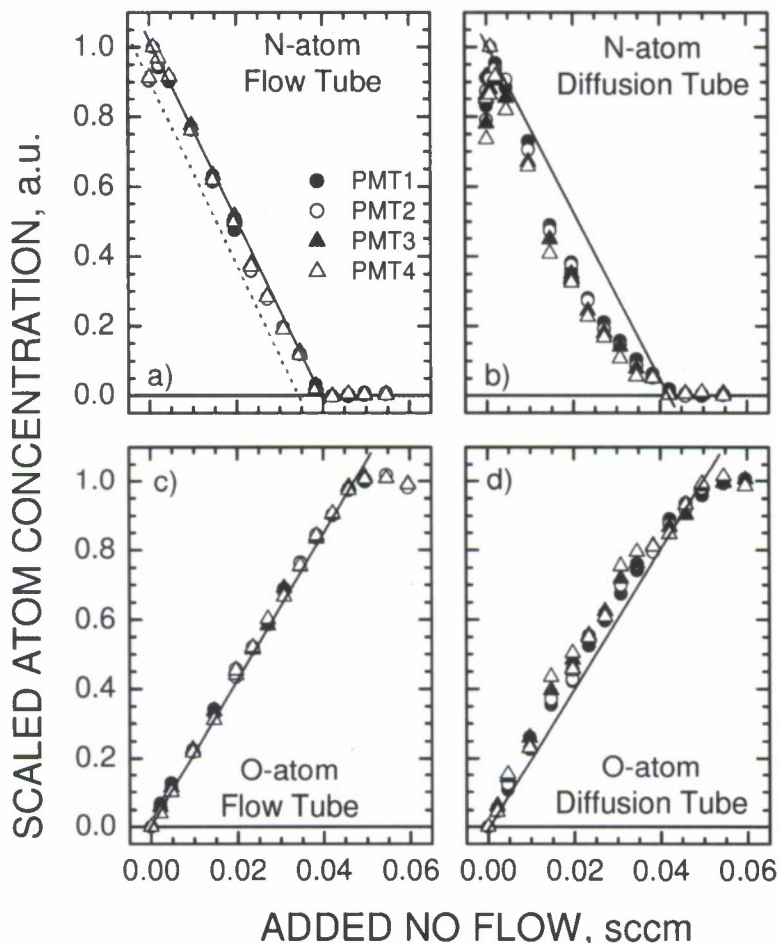


Figure 2. Important side-arm tube dimensions (in cm); drawing not to scale.

### Qualitative Behavior

Figures 3a-d show the variation in relative atom concentration as a function of the flow rate of NO added at the titration port for both N atoms and O atoms with the side-arm configured as either a flow tube or a diffusion tube. The raw LIF data collected by each PMT were corrected for scattered light contributions by subtracting the off-resonance signals (corrections were always 3% or less of the total signal), normalized by the square of the laser pulse energy, and averaged over at least 200 laser shots at each added NO flow setting. The averaged data reflect changes in atom concentration at the particular PMT location with NO additions at the titration port. To better illustrate common behaviors in Figs. 3a-d the averaged values were then put on a common scale by dividing each PMT data set by its maximum value.



**Figure 3.** Variations in the scaled atom concentrations measured at the four PMT locations with the addition of NO at the titration port: a) N atoms in flow tube, b) N atoms in diffusion tube, c) O atoms in flow tube, and d) O atoms in diffusion tube. Solid lines are guides for the eye; the offset dashed line in Fig 3a is discussed in the text.

With the side-arm tube configured as a flow tube, both the N-atom and the O-atom concentrations vary approximately linearly as NO is added at the titration port (except in the region near zero added NO in the N-atom figures; this is discussed in the following subsection.) When the reactor is switched to diffusion tube mode clear deviations from this linear dependence are evident.

In Fig. 3b the N-atom concentrations decrease faster with added NO, producing a concave profile, while in Fig. 3d the O-atom profile becomes convex, consistent with a faster rise in O-atom concentrations with added NO. The result shown in Fig. 3b reproduces the experimental observations of Copeland et al.<sup>11</sup> for N atoms, and the result shown in Fig. 3d confirms their predictions for O atoms. Copeland et al.<sup>11</sup> also found a trend of increasing deviation from linearity with increasing distance from the side-arm opening. Despite experimental scatter, similar trends are found in the present measurements, and especially when comparing PMT1 (solid circles) and PMT4 (open

triangles) data points near the midpoint of the titration curve. Thus, the current measurements support and strengthen the hypothesis of NO formation by surface reactions.

In order to compare experimental data with the predictions of a multi-species reaction-diffusion model, the scaled measurements of Figs. 3b and 3d must be corrected for variations in LIF detection sensitivities at the different PMT locations and the absolute atom concentrations at the side-arm opening must be determined.

### Concentration Estimates

Estimates of the atom concentrations at the side-arm opening can be made from the titration endpoints under flow tube conditions, however there are two complications: determining the exact endpoint and interpreting the initial rise of the N-atom signal with the addition of small amounts of NO (Fig 3a.)

The titration endpoints, where the N-atom LIF signal vanishes and the O-atom LIF signal levels off, are roughly 0.04 sccm NO in Fig. 3a and 0.045 sccm NO in Fig. 3c. This difference is likely a reflection of day-to-day repeatability (N-atom and O-atom measurements were conducted on different days), as well as experimental uncertainty associated with detecting a sharp endpoint.

Below the endpoint, the O-atom concentration rises linearly from zero with NO addition until the endpoint is reached where all atomic nitrogen has been consumed. Above the endpoint the O-atom concentration should remain constant. If we choose 0.0425 sccm NO as the average endpoint, the O-atom concentration is computed from the measured temperature, pressure and gas flows as  $\sim 2.11 \times 10^{-5} \text{ mol m}^{-3}$  with a 1- $\sigma$  uncertainty of  $\sim 25\%$ . It is shown in the following section, that O-atom losses on the walls between the titration port and side-arm entrance are small and easily absorbed in this error estimate.

If the  $\text{N} + \text{NO} \rightarrow \text{N}_2 + \text{O}$  reaction is the dominant reactive process, the O-atom endpoint concentration should also equal the N-atom number density without added NO. However, the N-atom concentration profiles in Figs. 3a and 3b show an initial sharp *increase* with the addition of small amounts of NO, in contrast to the immediate N-atom loss anticipated from the fast  $\text{N} + \text{NO}$  reaction. Similar behaviors have been documented by other researchers working with fast flow and/or high power nitrogen discharge systems.<sup>25-27</sup>

Two main explanations have been proposed: 1) NO addition causes a reduction in N-atom surface losses, or 2) NO addition catalyzes additional dissociation of electronically or vibrationally-excited nitrogen molecules,  $\text{N}_2^*$ . It is possible to construct kinetic models for both mechanisms that can mimic the experimental observations.<sup>25</sup>

In our system, NO is injected into the flow near the tube centerline and causes a very rapid rise in the N-atom LIF signal even when the concentration of NO is  $\sim 10$  times lower than the N-atom concentration. In order to decrease heterogeneous losses of N atoms either NO or the O atoms produced by  $\text{N} + \text{NO}$  reaction must reach the surface and dominate the competition for surface sites. It seems unlikely that NO could dominate surface coverage under these conditions, since N atoms are both in excess and should have a much stronger driving force (energy reduction) for chemisorption. Density functional theory computations by Arasa et al.<sup>28</sup>, suggest O atoms have a slightly greater adsorption energy on  $\text{SiO}_2$  than N atoms, but that both energies are high and initial sticking coefficients are similar.<sup>28</sup> More recent atomistic simulations of Cozmuta<sup>29</sup> predict that O-atom adsorption energies are higher than N-atom adsorption energies on silica surfaces and that O-atom adsorption dominates over N-atom adsorption in gas mixtures containing both species.

The present experiments were carried out at similar total pressures, temperatures and flow rates to those of Copeland et al.<sup>11</sup> who did not observe an initial rise in N-atom concentration with added NO. It is possible that Copeland et al. did not collect titration data with sufficient resolution in added NO flow to observe the initial N-atom signal rise. However our microwave discharge source also operates at much higher powers (2.4 kW vs. 100 W) and is expected to generate much higher concentrations of excited nitrogen species. Any reduction of N-atom surface recombination because of NO addition should be similar in both sets of experiments, however catalytic dissociation of N<sub>2</sub>\* upon NO addition would be more easily observed in our discharge system.

Within the catalytic dissociation model, the initial rise in the N-atom concentration is explained by a net reaction  $\text{NO} + \text{N}_2^* \rightarrow \text{NO} + \text{N} + \text{N}$ , where the reaction rate is faster than the  $\text{N} + \text{NO}$  rate. The subsequent N-atom concentration maximum and a linear decay with added NO is explained by the depletion of N<sub>2</sub>\*, the concentration of which is presumably lower at the titration port than that of N atoms. Since the slope of the linear decay then simply reflects removal of N atoms by NO, the endpoint corresponding to the initial N-atom concentration can be estimated from a parallel line (the dashed line in Fig. 3a) as approximately 0.035 sccm, or about 12.5% lower than the observed endpoint. The initial N-atom concentration corresponding to an average observed endpoint of 0.0425 sccm NO is then  $\sim 1.84 \times 10^{-5} \text{ mol m}^{-3}$ .

### LIF Signal Corrections

The LIF signal magnitudes collected from each PMT depend on many factors in addition to the local atom concentration, such as optical alignment, PMT sensitivity, filter transmission, and excitation volume and laser beam geometry. For a stable species, these factors can be determined for each PMT by filling the reactor with a uniform static concentration and comparing collected LIF signals, but this is not possible for reactive species like O and N atoms that are lost on the reactor walls. The closest approximation to uniform atom concentrations that can be obtained in our system is under flow tube conditions. However, the signal ratios collected in flow-tube mode still need to be adjusted for differences in atomic concentration at the different PMT locations caused by pressure gradients and heterogeneous atom losses, before they can be used to normalize diffusion tube measurements.

The Hagen-Poiseuille relation<sup>30</sup> can be used together with the ideal gas law, the measured pressures at ports A and B, the measured N<sub>2</sub> flow rates and the known reactor distances to compute the total gas pressure at each PMT location, assuming that molecular nitrogen dominates the transport properties with a viscosity of  $17.77 \times 10^{-6} \text{ Pa}\cdot\text{s}$  at 298 K.<sup>31</sup> The bulk flow speed,  $v$ , can be computed at each location from the pressure and N<sub>2</sub> flow rate, using mass conservation and the ideal gas law. The atom loss due to heterogeneous recombination between PMT locations are estimated from a simple one-dimensional first-order model that equates the difference in the atom flow between  $z$  and  $z + \delta z$  to the losses incurred on the wall over this distance. This model is described by the differential equation

$$\frac{d(vc)}{dz} = -\frac{\gamma \bar{v}}{2R} c, \quad (1a)$$

where  $R$  is the tube radius,  $c$  is the atom concentration,  $v$  is the bulk flow speed,  $\bar{v}$  is the average thermal speed of the atoms  $\sqrt{8\mathcal{R}T/\pi M}$ , and  $\gamma$  is the estimated loss probability (the fraction of atom-

surface collisions which result in permanent removal of the atom from the gas phase). The value of  $\gamma$  is uncertain, but as a first approximation can be taken in the range  $\sim 1-10 \times 10^{-5}$  for O and N atoms on quartz.<sup>14</sup> Defining the representative atom concentration over  $\delta z$  as  $\bar{c} \equiv vc/v_{ave}$  allows integration of Eq. (1a) to give

$$\frac{c(z_1)}{c(z_2)} = \frac{v_2}{v_1} \exp\left(-\frac{\gamma \bar{v}(z_2 - z_1)}{2Rv_{ave}}\right) = \frac{P_1}{P_2} \exp\left(-\frac{\gamma \bar{v}(z_2 - z_1)}{2Rv_{ave}}\right), \quad (1b)$$

where  $v_{ave}$  is the average flow velocity between locations  $z_1$  and  $z_2$ , and  $v_2/v_1 = P_1/P_2$  follows from the ideal gas law and mass conservation. Eq. (1b) allows estimation of the combined effects of pressure difference and wall loss on the local atom concentrations between two PMT positions along the flow tube.

For N-atom LIF calibration, flow tube measurements were made without added NO flow. For O-atom LIF calibration, NO was added just below the titration endpoint. Table 1 lists the pressure ratios for the different PMT locations under our flow conditions, as well as the estimated ratios of atom concentration for different assumed values of  $\gamma$ . Pressure variations are small, amounting to only a few percent. However, wall losses can potentially change the atom concentrations by several 10's of percent along the flow tube, depending on the loss probabilities assumed. We choose the value  $\gamma_o = \gamma_N = 1 \times 10^{-5}$  in our estimates of wall loss and show later that this produces reasonable agreement between simulations and experiment. Table 2 compares the measured PMT signal ratios in flow tube mode to the pressure and wall loss corrected PMT signal ratios.

**Table 1. Calculated pressure and concentration ratios in flow tube configuration**

| PMT | Pressure Ratios | N-atom Concentration Ratios   |                    |                    | O-atom Concentration Ratios   |                    |                    |
|-----|-----------------|-------------------------------|--------------------|--------------------|-------------------------------|--------------------|--------------------|
|     |                 | $\gamma_N = 1 \times 10^{-5}$ | $5 \times 10^{-5}$ | $1 \times 10^{-4}$ | $\gamma_o = 1 \times 10^{-5}$ | $5 \times 10^{-5}$ | $1 \times 10^{-4}$ |
| 1   | 1               | 1                             | 1                  | 1                  | 1                             | 1                  | 1                  |
| 2   | 0.982           | 0.979                         | 0.900              | 0.809              | 0.980                         | 0.906              | 0.821              |
| 3   | 0.964           | 0.959                         | 0.811              | 0.658              | 0.962                         | 0.822              | 0.676              |
| 4   | 0.946           | 0.940                         | 0.733              | 0.537              | 0.943                         | 0.747              | 0.559              |

**Table 2. Measured and corrected PMT signal ratios in flow tube configuration**

| PMT | N-atom PMT Signal Ratios |           | O-atom PMT Signal Ratios |           |
|-----|--------------------------|-----------|--------------------------|-----------|
|     | Measured                 | Corrected | Measured                 | Corrected |
| 1   | 1                        | 1         | 1                        | 1         |
| 2   | 1.06                     | 1.10      | 1.21                     | 1.26      |
| 3   | 2.90                     | 3.14      | 3.53                     | 3.81      |
| 4   | 0.694                    | 0.780     | 0.565                    | 0.633     |

Relative atom concentrations during diffusion tube experiments can now be assigned by dividing the LIF data by the corrected PMT signal ratios of Table 2. Figures 4a and 4b show these relative atom concentrations as a function of added NO flow, for N atoms and O atoms, respectively, where the data have been adjusted to the same endpoint of 0.0425 sccm added NO flow. The corresponding N- and O-atom concentrations at the side-arm entrance can be approximated by the expressions  $c_O = 2.11 \times 10^{-5} F_{NO}/0.0425$  and  $c_N = 2.11 \times 10^{-5} (0.0425 - F_{NO})/0.0415$ , where concentrations are in  $\text{mol m}^{-3}$  and NO flows are in sccm.

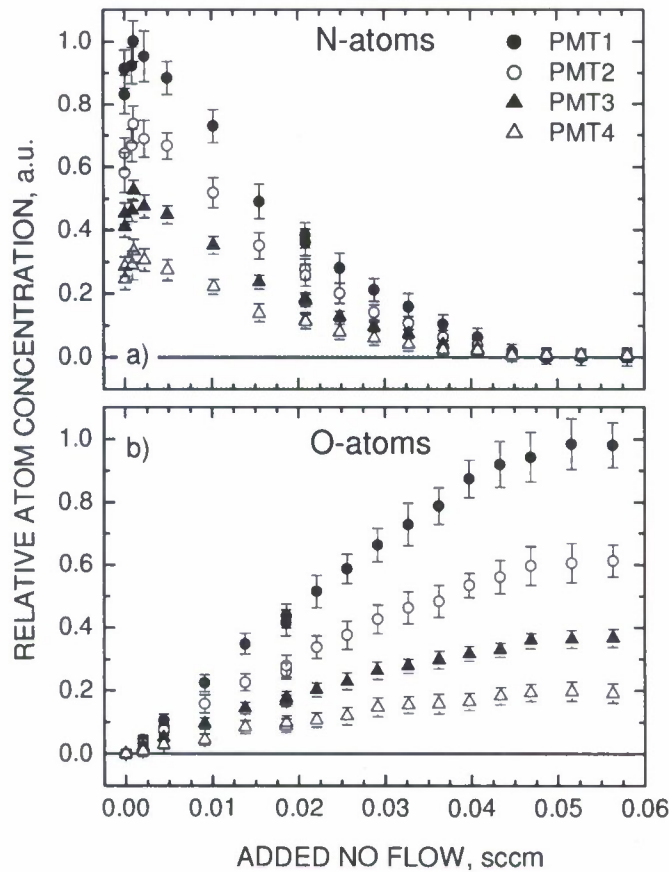


Figure 4. Relative atom concentrations at the different PMT locations during diffusion tube experiments: a) N atoms, and b) O atoms. The error bars are the standard deviations of the collected PMT signals.

## Reactor Modeling

A numerical reaction-diffusion model was developed at Princeton to try to reproduce the curvatures and relative magnitudes of the experimental N- and O-atom concentrations plotted in Fig. 4, and the corresponding scaled measurements in Fig. 3, using the entrance atom concentrations deduced above and various surface reaction boundary conditions. The side-arm reactor geometry was modeled as tube of length  $L = 146.7$  cm and uniform radius  $R = 1.1$  cm, closed at one end by a disk normal to the tube axis. The governing equation describing two-dimensional cylindrical diffusion-reaction of species  $s$  in the side-arm tube is

$$\frac{\partial \rho_s}{\partial t} + \frac{1}{r} \frac{\partial}{\partial r} (r j_{sr}) + \frac{\partial}{\partial z} (j_{sz}) = w_s \quad (2)$$

where  $\rho_s$  is the species mass density,  $w_s$  represents the rate of species production due to gas-phase chemical reactions, and  $j_{sr}$  and  $j_{sz}$  are the diffusive mass fluxes in the radial and axial directions relative to the mass average velocity of the mixture. The diffusive mass fluxes in the radial and axial directions are related to the corresponding diffusion velocities by  $j_{sr} = \rho_s v_{sr}$  and  $j_{sz} = \rho_s v_{sz}$ .

Concentration profiles were obtained by the simultaneous solution of the set of 8 species continuity equations (Eq. 2) for N, O, N<sub>2</sub>, O<sub>2</sub>, NO, N<sub>2</sub>O, NO<sub>2</sub>, and O<sub>3</sub>. Solution of the momentum and energy equations is not required to obtain concentration profiles under the isothermal and isobaric conditions of the dead-end side-arm reactor. The ideal gas law was used as the equation of state. The species mass flux vector is given by

$$\mathbf{j}_s = -(cM_s D_s) \nabla x_s + \frac{\rho_s}{\rho} \sum_r (cM_r D_r) \nabla x_r \quad (3)$$

with  $M_s$  the species molar mass,  $x_s$  the species mole fraction, and  $D_s$  the effective binary diffusion coefficient for species  $s$  in the gas mixture;  $c$  and  $\rho$  are the total molar and mass densities of the gas, respectively.

Effective diffusion coefficients in the multi-component gas mixtures of the experiment are computed using the friction-weighted self-consistent effective binary diffusion (SCEBD) approximation<sup>32,33</sup>:

$$D_s = \left( 1 - \frac{\omega_s}{\omega} \right) \left( \sum_{r \neq s} \frac{x_r}{D_{r,s}} \right)^{-1} \quad (4)$$

Different choices are possible for the weighting factor  $\omega_s^{32,33}$ ; we choose  $\omega_s = x_s$  so that Eq. 4 reduces to the exact binary value for a two-component mixture. The binary diffusion coefficients  $D_{r,s}$  for all species pairs are computed from

$$D_{r,s} = \frac{3}{16P\pi\bar{\Omega}_{rs}^{(1,1)}} \sqrt{\frac{2\pi(k_B T)^3 N_{Avro}}{M_{r,s}}}, \quad (5)$$

where  $M_{r,s} = M_r M_s / (M_r + M_s)$  and  $\bar{\Omega}_{rs}^{(1,1)}$  are collision integrals compiled by Wright et al.<sup>34,35</sup>. The collision integrals were implemented using the curve fit formulas of Gupta et al.<sup>36</sup>, in a manner identical to that employed in the widely used NASA CFD code, DPLR.<sup>37</sup> Collision integrals for ozone were unavailable, and were approximated by those given for carbon dioxide. Table 3 lists the room-temperature rate coefficients for nine gas phase reactions included in our model involving dissociated oxygen and nitrogen species. The reverse reaction rates are negligibly slow under our experimental conditions and were set to zero.

**Table 3. Gas-phase reactions**

|    | Reaction                          | Rate <sup>a</sup>                       | References |
|----|-----------------------------------|---|------------|
| R1 | $O + O + M \rightarrow O_2 + M$   | $k_1 = (3.1 \pm 1.6) \times 10^{-33}$   | 38         |
| R2 | $O + O_2 + M \rightarrow O_3 + M$ | $k_2 = (6.0 \pm 0.6) \times 10^{-34}$   | 20         |
| R3 | $O + O_3 \rightarrow O_2 + O_2$   | $k_3 = (8.0 \pm 1.2) \times 10^{-15}$   | 20         |
| R4 | $O + N + M \rightarrow NO + M$    | $k_4 = (1.0 \pm 0.5) \times 10^{-32}$   | 21         |
| R5 | $O + NO + M \rightarrow NO_2 + M$ | $k_5 = (9.0 \pm 1.8) \times 10^{-32}$   | 20         |
| R6 | $O + NO_2 \rightarrow NO + O_2$   | $k_6 = (1.04 \pm 0.15) \times 10^{-11}$ | 20         |
| R7 | $N + N + M \rightarrow N_2 + M$   | $k_7 = (4.4 \pm 2.2) \times 10^{-33}$   | 21         |
| R8 | $N + NO \rightarrow N_2 + O$      | $k_8 = (3.0 \pm 0.9) \times 10^{-11}$   | 20         |
| R9 | $N + NO_2 \rightarrow N_2O + O$   | $k_9 = (1.2 \pm 0.6) \times 10^{-11}$   | 20         |

<sup>a</sup> Bimolecular rate constants are in units of  $\text{cm}^3 \text{ molecule}^{-1} \text{ s}^{-1}$ . Termolecular rate constants are in units of  $\text{cm}^6 \text{ molecule}^{-2} \text{ s}^{-1}$ , and the collision partner M is taken as  $N_2$ .

The production of species by surface-catalyzed reactions must be balanced by their diffusive flux at the wall:

$$-j_{s,w} = w_{s,w} \quad (6)$$

For *reactant* species the production rates at the surface can be expressed as a loss probability,  $\gamma_s$ , times the surface impingement fluxes; for O and N atoms this gives the production rates (negative for loss)

$$w_{O,w} = -\gamma_O \frac{\rho_{O,w} \bar{v}_O}{4} \quad (7a)$$

$$w_{N,w} = -\gamma_N \frac{\rho_{N,w} \bar{v}_N}{4} \quad (7a)$$

The loss probability is defined as *the fraction of impinging reactant flux removed permanently from the gas phase*. It is not a fundamental chemical quantity, rather, it reflects the total efficiency of all operating surface reaction pathways that remove species  $s$  on a particular surface under a particular combination of temperature, pressure, and gas composition. If the reactant species is consumed to produce more than one product species, branching fractions,  $f_{s,r}$ , can be defined as *the fraction of impinging reactant removed permanently from the gas phase that participates in forming product species  $r$* . We avoid the common term “recombination coefficient” for  $\gamma_s$  because this term implies a reaction product that is the parent molecule of the reactant (i.e.,  $O_2$  for O-atoms), which is clearly not always the case in multi-reactant mixtures.

The absolute lower and upper bounds on both  $\gamma_s$  and  $f_{s,r}$  are 0 and 1, but this range may be reduced by other factors such as the availability of partner reactants. For a partially dissociated mixture of oxygen and nitrogen interacting with a catalytic surface via three net steady-state heterogeneous reaction pathways:  $O + O \rightarrow O_2$ ,  $N + N \rightarrow N_2$ , and  $O + N \rightarrow NO$ , element conservation dictates the constraint:

$$(1 - f_{O,O_2}) \gamma_O \rho_{O,w} \bar{v}_O / M_O = (1 - f_{N,N_2}) \gamma_N \rho_{N,w} \bar{v}_N / M_N \quad (8)$$

In the simulations that follow, we demonstrate the effect of NO surface production on the predicted O- and N-atom concentration profiles along the diffusion side-arm tube for different fixed  $N_2/N/O$  compositions at the side-arm opening. To achieve this we choose values of  $\gamma_O$  and  $\gamma_N$ , and then vary nitric oxide surface production. When  $\gamma_O \rho_{O,w} \bar{v}_O / M_O < \gamma_N \rho_{N,w} \bar{v}_N / M_N$ , the level of NO production can be set by choosing  $0 \leq f_{O,O_2} \leq 1$  together with

$$f_{N,N_2} = 1 - (1 - f_{O,O_2}) (\gamma_O \rho_{O,w} \bar{v}_O M_N / \gamma_N \rho_{N,w} \bar{v}_N M_O) \quad (9a)$$

When  $\gamma_O \rho_{O,w} \bar{v}_O / M_O > \gamma_N \rho_{N,w} \bar{v}_N / M_N$ , NO production is determined by choosing  $0 \leq f_{N,N_2} \leq 1$  and

$$f_{O,O_2} = 1 - (1 - f_{N,N_2}) (\gamma_N \rho_{N,w} \bar{v}_N M_O / \gamma_O \rho_{O,w} \bar{v}_O M_N) . \quad (9b)$$

Nitric oxide surface production is respectively eliminated or maximized when  $f_{O,O_2} = 1$  or 0 in Eq. (9a), or when  $f_{N,N_2} = 1$  or 0 in Eq. (9b).

The individual production rates of the surface reaction products are

$$w_{O_2,w} = -f_{O,O_2} \frac{M_{O_2}}{2M_O} w_{O,w} \quad (10a)$$

$$w_{N_2,w} = -f_{N,N_2} \frac{M_{N_2}}{2M_N} w_{N,w} \quad (10b)$$

$$w_{NO,w} = (f_{N,N_2} - 1) \frac{M_{NO}}{M_N} w_{N,w} = (f_{O,O_2} - 1) \frac{M_{NO}}{M_O} w_{O,w} . \quad (10c)$$

Equation (6), together with expressions (7a,b) and (10a-c), provides the species boundary conditions on all the side-arm surfaces at  $r = R$  for  $z = 0$  to  $L$  and at  $z = L$  for  $r = 0$  to  $R$ . A zero-flux boundary condition,  $j_{sr} = 0$ , was applied along the tube centerline ( $r = 0$  for  $z = 0$  to  $L$ ). The gas composition at the side-arm entrance was specified according to the experimental conditions and taken as uniform for  $z = 0$  and  $r = 0$  to  $R$ .

Equation 2 was discretized using a fourth-order accurate finite difference scheme for the spatial derivatives and iterated to steady-state using a third-order accurate Runge-Kutta method. Grid convergence was obtained for grids with  $60 \times 10$  grid points in the axial and radial directions, respectively. Steady-state solutions were achieved using a CFL (Courant, Freidricks, Levy) number of 1. The CFL number is defined as the ratio of the simulation time step,  $\Delta t$ , to the minimum physical diffusion time scale in the flow,  $\Delta t_{diff}$ , where  $\Delta t_{diff} = \rho(\Delta z^2 + \Delta r^2) / \mu$  and  $\Delta z$  and  $\Delta r$  are the grid spacings in the axial and radial directions, respectively. The simulations that follow were all computed using a  $60 \times 10$  grid and a CFL number of 1.

### Simulation Results

Simulations were computed for  $T = 298$  K,  $P = 60$  Pa, and various O-atom and N-atom concentrations at the side-arm entrance corresponding to NO titration flows in the range 0.0 to 0.0425

sccm, with the balance assumed to be molecular nitrogen. The concentrations of all other species were set to zero at the entrance.

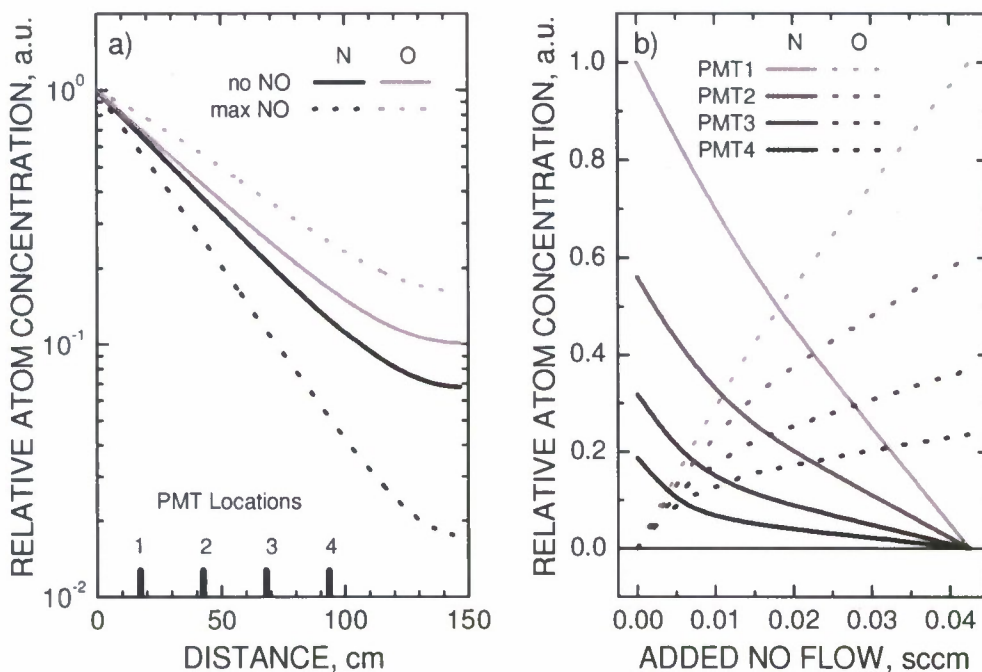


**Figure 5.** Model simulations for  $\gamma_O = \gamma_N = 1 \times 10^{-5}$ : a) relative atom concentration profiles along the diffusion tube side-arm at an added NO flow rate of 0.0215 sccm, with or without surface NO production; b) relative atom concentrations at different PMT locations as a function of the flow of added NO, with maximum NO surface production.

Figure 5a shows relative atom concentration profiles along the dead end diffusion tube computed for an NO titration flow of 0.0215 sccm and the loss probabilities  $\gamma_O = \gamma_N = 1 \times 10^{-5}$ . The solid lines show the decay of N- and O-atom concentrations along the diffusion tube when no surface NO production is allowed. Though the loss probabilities are set equal for N and O atoms in this simulation, N atoms are lost more rapidly down the side-arm tube than O atoms because the lighter N atoms collide with the surface more often and have a lower diffusion coefficient in molecular nitrogen (about 522 vs. 628 cm<sup>2</sup> s<sup>-1</sup>). The corresponding profiles when NO surface production is maximized (dotted lines), show that the loss rate of N atoms increases and the loss rate of O atoms decreases.

With surface NO production eliminated, the same concentration profiles (Fig. 5a, solid lines) are produced whether or not gas-phase chemistry is included in the computations. With surface NO production maximized and the N + NO gas phase reaction eliminated, computed O- and N-atom profiles again overlay the profiles for no NO surface production (solid lines). Taken together, these modelling results support the mechanism proposed by Copeland et al.<sup>11</sup>, that requires both surface production of NO and the N + NO gas-phase reaction to explain the experimental measurements.

In Fig. 5b, we show the relative N-atom (solid lines) and O-atom (dotted lines) concentrations computed at the different PMT locations as a function of added NO flow. These computations were made assuming maximum NO surface production and  $\gamma_O = \gamma_N = 1 \times 10^{-5}$ . Comparison with the experimental data of Fig. 4 shows generally good agreement, keeping in mind that the initial rise of N-atoms with NO addition is not included in the reaction-diffusion model. Relative atom concentrations under un-titrated and fully-titrated conditions are independent of surface or gas-phase NO chemistry. Model predictions using  $\gamma_O = \gamma_N = 1 \times 10^{-5}$  reproduce measured relative atom concentrations at 0.0 and 0.0425 sccm added NO fairly well. Much poorer agreement is obtained for higher loss probabilities like  $\gamma_O = \gamma_N = 5 \times 10^{-5}$  which predict atom losses much greater than those observed experimentally.

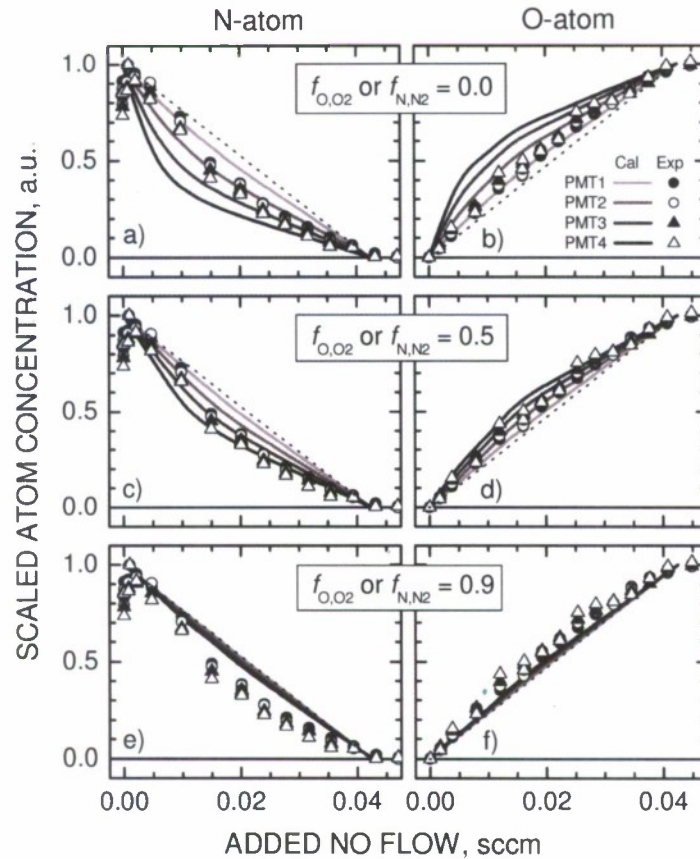


**Figure 6.** Experimental (symbols) and computed (lines) scaled atom concentrations at the four PMT locations as functions of added NO flow. Computations with  $\gamma_O = \gamma_N = 1 \times 10^{-5}$  and a), b) maximum, c), d) intermediate, and e), f) minor NO surface production. Dotted lines show a linear dependence for reference.

Figures 6a-f compare experimental scaled N-atom and O-atom concentrations to numerical predictions assuming  $\gamma_O = \gamma_N = 1 \times 10^{-5}$  and different levels of NO surface production. The

experimental data have been scaled to align (approximately) the experimental and computational endpoints at 0.0 sccm (no O atoms) and 0.0425 sccm (no N atoms).

Figures 6a and 6b show that the model computations with maximum NO surface production reproduce the concave and convex curvatures observed in the experimental diffusion tube data for both N and O atoms. However, the predicted differences in curvature between four PMT locations are much larger than observed, suggesting that the maximum surface NO production condition is too extreme.

A similar comparison is shown in Figs. 6c and 6d, for calculations that enforce a more moderate NO surface production condition, by setting either  $f_{O,O_2} = 0.5$  in Eq. 9a or  $f_{N,N_2} = 0.5$  in Eq. 9b. The computed profiles now show a tighter spread in curvature, more in line with experimental observation, especially for oxygen atoms. While the quality of agreement depends somewhat on the scaling used to align the experimental and computed endpoints, the general observations of the experiment are well reproduced.

Figures 6e and 6f show computational results when NO surface production is a minor pathway (either  $f_{O,O_2} = 0.9$  in Eq. 9a or  $f_{N,N_2} = 0.9$  in Eq. 9b.) The profiles show much less curvature, approaching the linear dependence indicated by the dotted line, and compress the differences in curvature between the four PMT locations further. These simulations do not reproduce the experiment as well as those of Figs 6c and 6d, indicating that NO surface production is not a minor pathway in our experiment, but rather comparable in magnitude to the O + O and N + N surface recombination pathways.

The reaction-diffusion model used to simulate the diffusion tube experiments is only constrained by element conservation and does not include finite rate surface chemistry. This type of model is often used for parametric studies seeking to bound catalytic effects<sup>39</sup>, but lacks physics-based kinetic formulations that describe intermediate catalytic behavior under transient thermal and flow environments. A more attractive approach for including the NO surface formation in CFD computations is with a finite-rate surface chemistry model as implemented by Kurotaki<sup>7</sup> and others<sup>3-6,8,9</sup>; i.e., a model that incorporates kinetic mechanisms like adsorption, thermal desorption, Eley-Rideal recombination and Langmuir-Hinshelwood recombination. Unfortunately, these models contain large numbers of numerical parameters that must be chosen by theory and/or adjusted to reproduce experiment data. More experimental data are required, at higher temperatures and over a larger range of gas pressures and compositions, to enable the construction of a suitable finite-rate chemistry model.

Nevertheless, the experimental results presented here support the surface-catalyzed production of nitric oxide from the recombination of atomic oxygen and atomic nitrogen on quartz surfaces. Computational simulations of the side-arm reactor with a multi-species reaction-diffusion model, incorporating NO surface production and gas phase reaction of NO and N atoms, qualitatively reproduce the experimental observations, and suggest that NO surface formation is of comparable magnitude to the O + O and N + N surface recombination reactions.

## SURFACE PRODUCTION OF NITRIC OXIDE AT ELEVATED TEMPERATURES: EXPERIMENTS USING DIRECT DETECTION OF NO

The experimental approach we used to infer the production of NO on silica surfaces at room temperature can in principle be extended to elevated temperatures. However, at elevated temperatures such experiments encounter significant complications. The primary difficulty is the rapidly increasing intensity of the blackbody radiation with increasing furnace temperature, which creates a massive signal background in the 745 nm and 845 nm observation windows used to detect N and O atoms by 2-photon LIF. The atom number densities in the diffusion tube at high temperatures are lower than at room temperature because of the ideal gas law,  $N_{High} = N_{Low} [T_{Low}/T_{High}]$  at constant pressure. In addition, the heterogeneous loss of atoms on hot silica walls generally increases with temperature and the LIF scheme for O-atoms probes the population of the ground state with the  $J = 2$  fine structure component, which also decreases with rising temperature.<sup>22,23</sup> Thus, extracting small LIF signals from the overwhelming thermal radiation background at high temperature becomes extremely challenging.

We have developed a new experimental method for the investigations of NO surface production at elevated temperatures, based on the direct detection of NO by single-photon LIF combined with photon counting. Surface-produced NO molecules are rapidly lost in the gas-phase by the reaction  $\text{NO} + \text{N} \rightarrow \text{N}_2 + \text{O}$ ; however, the steady-state NO densities resulting from the balance between the surface production and phase-phase reaction loss are still well within the reach of sensitive single-photon LIF detection. The LIF from NO is observed in the ultraviolet spectral region, thus thermal radiation background from the hot furnace has a much smaller effect than in the near-infrared. As an added advantage, NO signal detection actually becomes easier at elevated temperatures, because the NO surface production is expected to become more efficient, while the rate coefficient for NO removal by  $\text{NO} + \text{N} \rightarrow \text{N}_2 + \text{O}$  decreases with increasing temperature<sup>20</sup>.

The experimental setup is very similar to the one described previously and shown in Fig. 1, with the following differences. For NO detection, we use two Hamamatsu R928 PMTs mounted at different distances along the diffusion tube. Compared to the R636 PMTs used for N- and O-atom LIF detection, the R928 PMTs have a higher sensitivity in the ultraviolet and a greater internal gain, which makes them more suitable for photon-counting detection of the 248 nm LIF from NO. Instead of the gated integrators, we use two SRS SR400 photon counters to record the PMT signals, which allow us to work with fluorescence signals lower than 1 photon per laser pulse. LIF was induced by laser output with wavelengths near 226 nm, corresponding to the  $A-X(0,0)$  band of NO, and fluorescence was detected near 248 nm ( $A-X(0,1)$  band) using PMTs filtered by 248 nm interference filters with a FWHM of 10 nm. To avoid saturation effects that would cause nonlinearities of the measured LIF signal with respect to the excitation energy, the excitation laser beam was attenuated using a Schott colored glass filter (2 mm-thick UG-5).

The main difficulty we faced using this new approach was to discriminate between the desired signal - that of the surface-produced NO - and background signals from NO present in the system from other sources. We have addressed this problem by employing isotopically-enriched titration gases as described below.

The first complication arises from the fact that the titration agent is the same species as the one whose surface production is investigated. The titration endpoint is never particularly sharp, in part due to instabilities in the gas flows, implying that, below but near the titration endpoint, the surface-produced NO signal will be superposed with the emerging signal from the NO titration gas that was

not completely consumed in the gas-phase reaction with N atoms. This makes it impossible to discern the behavior of the surface-produced NO signal near the endpoint.

To bypass this problem, we used NO gas labeled by the  $^{15}\text{N}$  isotope, as the titration agent. The main flow of nitrogen gas passing through the discharge produces  $^{14}\text{N}$  atoms and the  $^{15}\text{N}$  atoms from the  $^{15}\text{NO}$  titration gas are incorporated into  $^{15}\text{N}^{14}\text{N}$  molecules during the titration reaction. Any residual titration gas in the system would be  $^{15}\text{NO}$  and any surface-produced nitric oxide molecules would be  $^{14}\text{NO}$ . The measured rotationally-resolved LIF excitation spectra of  $^{15}\text{NO}$  and  $^{14}\text{NO}$  are different and it is easy to trace the evolution of LIF signals of both species with the changes in the flow rate of the titration gas. (The natural ratio  $^{14}\text{N}/^{15}\text{N}$  is about 270 so strictly speaking some  $^{15}\text{N}$  is generated in discharge and some  $^{15}\text{NO}$  could be produced on the surface, but these levels would be more than two orders of magnitude smaller than surface produced  $^{14}\text{NO}$ .)

Gas-phase exchange reactions between isotopically-labelled nitrogen atoms and nitrogen molecule or nitric oxide molecules would complicate the interpretation of these experiments. Fortunately the rates for these exchange reactions turn out to be extremely slow. Back and Mui<sup>40</sup> have set an upper limit for the rate constant of the reaction  $^{14}\text{N} + ^{15}\text{N}^{15}\text{N} \rightarrow ^{15}\text{N} + ^{14}\text{N}^{15}\text{N}$  of  $6.6 \times 10^{-16} \text{ cm}^3 \text{ molecule}^{-1} \text{ s}^{-1}$  at a temperature of  $1000^\circ\text{C}$ . The exchange reaction rate decreases with decreasing temperature and so the rate constant should be even smaller near room temperature.<sup>41,42</sup> Back and Mui<sup>40</sup> also set the upper limit for the exchange reaction  $^{14}\text{N} + ^{15}\text{NO} \rightarrow ^{15}\text{N} + ^{14}\text{NO}$  to be at least 250 times slower than the rate of the  $^{14}\text{N} + ^{15}\text{NO} \rightarrow \text{O} + ^{14}\text{N}^{15}\text{N}$  reaction, based on experiments at both room temperature and  $380^\circ\text{C}$ .

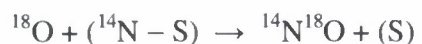
A second, somewhat perplexing complication arose because of a background NO LIF signal observed at elevated temperatures, even without any titration gas added into the system, indicating that a source of oxygen atoms other than the NO titration agent was present in the system. This background signal was only observed with the microwave discharge running and was found to increase as the furnace temperature rose. The immediate suspects were an  $\text{O}_2$  impurity in the  $\text{N}_2$  gas or an air leak into the system, both of which could lead to the production of O atoms in the discharge. We replaced the standard 99.999% purity  $\text{N}_2$  gas (<1 ppm specified  $\text{O}_2$  impurity) by a special  $\text{N}_2$  grade with specified  $\text{O}_2$  impurity less than 0.01 ppm, however the background NO signal remained as large as before, demonstrating that  $\text{O}_2$  impurity in the  $\text{N}_2$  gas was not the source. We were unable to find any leaks into the system using a He leak detector, however the base pressure of the evacuated system once isolated from the pump did slowly rise either from out-gassing of the system walls or from some undiscovered leak.

In a separate experiment, small amounts of air were added at the titration inlet at flow rates ( $\sim 0.2 \text{ sccm}$ ) that produced pressure rises similar to the natural pressure rises in the isolated evacuated system. These air additions increased the NO background signal by factors 2 to 4. This experiment shows that the oxygen impurity need not be introduced upstream of the discharge to act as a source of O-atoms. It is possible, though unlikely, that some  $\text{O}_2$  can diffuse against the bulk flow to dissociate in the discharge. Another possibility is that O atoms are created by gas-phase reactions of  $\text{O}_2$  with electronically excited nitrogen molecules, particularly  $\text{N}_2$  (A) and  $\text{N}_2$  (B), created by the discharge or by  $\text{N} + \text{N}$  gas-phase recombination in the post-discharge region.<sup>43,44</sup>

Being unable to eliminate the background NO signal, we resorted again to the isotopic labeling approach, this time also labeling the O atoms of the titration NO gas by the  $^{18}\text{O}$  isotope. The titration reaction now becomes



The surface reactions involving N atoms generated in the discharge and O atoms originating from the titration gas now become



Therefore, we assured that the detected  $^{14}\text{N}^{18}\text{O}$  nitric oxide has an O atom that *is* provided by the titration gas, and an N atom that *is not* provided by the titration gas. The atomic purities of the isotopically labeled gases we used are (99% N, 98% O) for  $^{15}\text{N}^{18}\text{O}$  and 98%+ N for  $^{15}\text{N}^{16}\text{O}$ . The natural  $^{16}\text{O}/^{18}\text{O}$  ratio is about 500.

The measurement protocol was as follows. Upon heating the furnace to a target temperature, we first measured the LIF excitation spectrum with discharge running at full power and without added NO titration agent. The spectrum was collected by slowly scanning the dye laser wavelength while counting photons in both PMT channels for a number (10–50) of laser pulses. The counting period was selected such that it did not diminish the wavelength resolution of the spectrum. For all elevated temperatures, the spectrum showed features easily assigned to  $^{14}\text{N}^{16}\text{O}$ , which constitute the background signal discussed in the text above.

Isotopically labeled NO titration gas was then introduced and the spectrum was re-measured at different flow rates. The titration flow rate was increased in small increments until the endpoint was passed as indicated by the disappearance of the surface-produced NO signal and the appearance of the LIF signal from the NO species introduced by titration.

Finally, we performed the calibration step: the discharge was turned off, NO was introduced in the system with a known flow rate, and its spectrum was measured. The calibration has two roles. First, it serves to cross-calibrate the two PMTs, which have different sensitivity factors. Those factors can be determined by comparing the PMT signals in the calibration run, when both PMTs detect LIF corresponding to the same NO number density. Second, the LIF signal strength from a known NO number density can be used to extract the absolute number density of the surface-produced NO by comparison.

Ideally  $^{14}\text{N}^{18}\text{O}$  would be used for this calibration step, since this is the species produced by surface reaction in the experiments with the  $^{15}\text{N}^{18}\text{O}$  titration gas. Unfortunately  $^{14}\text{N}^{18}\text{O}$  was not commercially available during the timeframe of this study. Therefore we use experiments with  $^{15}\text{N}^{18}\text{O}$  titration gas to determine the general trends of the (unambiguously) surface-produced  $^{14}\text{N}^{18}\text{O}$  number density as a function of titration gas flow rate. Absolute values of the surface-produced NO number density at different elevated temperatures were determined separately from  $^{15}\text{N}^{16}\text{O}$  titration experiments that generated  $^{14}\text{N}^{16}\text{O}$ . The LIF signals collected during these experiments were corrected by subtracting the background  $^{14}\text{N}^{16}\text{O}$  signals discussed above and then comparing the signal strength to calibration measurements using standard  $^{14}\text{N}^{16}\text{O}$  gas (10% NO balance  $\text{N}_2$ ). This procedure adds some uncertainty to the results.

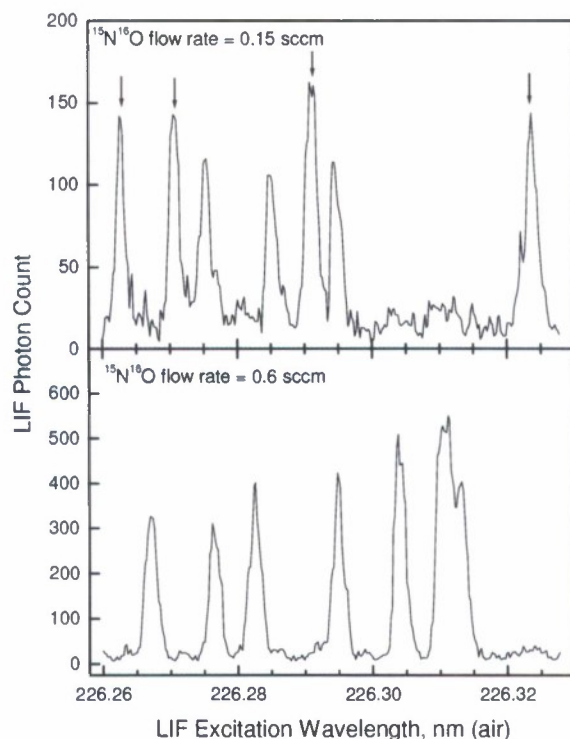


**Figure 7.** LIF spectra at 1000 K obtained using  $^{15}\text{N}^{16}\text{O}$  titration. The spectra were measured at a distance of 100 cm down the diffusion tube and represent the sum photon count for 40 laser pulses. **Top:** spectrum measured below the titration endpoint, showing lines of  $^{14}\text{N}^{16}\text{O}$ . The lines that were used to calculate the changes of LIF intensities with the titration flow rate (Fig. 8) are labeled by arrows. **Bottom:** spectrum measured above the titration endpoint, showing lines of  $^{15}\text{N}^{16}\text{O}$ .

To minimize the data acquisition time, we scanned the dye laser wavelength over relatively narrow spectral regions that contain several well-separated lines of each of the NO species of interest. Figure 7 shows spectra collected in the experiments at 1000 K using  $^{15}\text{N}^{16}\text{O}$  as the titration agent. Below the endpoint (observed at a  $^{15}\text{N}^{16}\text{O}$  flow rate of  $\sim 0.57$  sccm), the spectrum shows practically only  $^{14}\text{N}^{16}\text{O}$  features; the very weak  $^{15}\text{N}^{16}\text{O}$  features in the 226.30–226.32 nm range may be due to residual  $^{15}\text{N}^{16}\text{O}$  left over in the diffusion tube from the previous run above the endpoint, or partly due to  $^{15}\text{N}^{16}\text{O}$  naturally present in the  $^{14}\text{N}^{16}\text{O}$  cylinder. The spectrum shows raw photon count, and it illustrates the size of the background blackbody radiation signal relative to the LIF signal. Above the endpoint, only strong  $^{15}\text{N}^{16}\text{O}$  features are observed (bottom spectrum at Fig. 7). For either species, there are several lines that are well separated from the lines of the other species and can be used unambiguously for species identification.

After normalizing the spectrum by dividing the signal with the measured laser pulse energy, 4 well-separated  $^{14}\text{N}^{16}\text{O}$  lines were fitted with Gaussians and the sum area of the 4 Gaussians was used to trace the dependence of the  $^{14}\text{N}^{16}\text{O}$  LIF signal on the titration gas flow rate. This dependence is shown in Figure 8, in which absolutely calibrated signals for both PMTs are plotted. Starting from a non-zero value at zero  $^{15}\text{N}^{16}\text{O}$  flow, the  $^{14}\text{N}^{16}\text{O}$  number density increases up to about 0.45 sccm, and then rapidly falls towards zero as the flow rate approaches the endpoint value.

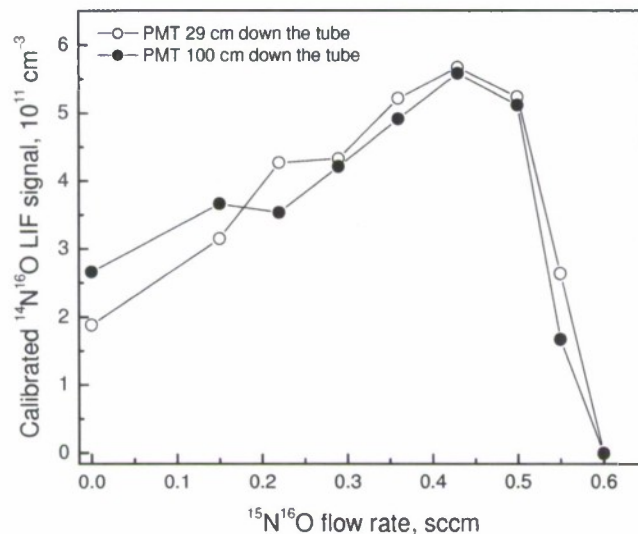


**Figure 8.** LIF signal intensity for  $^{14}\text{N}^{16}\text{O}$  as a function of the  $^{15}\text{N}^{16}\text{O}$  titration flow rate. Measurements were performed at 1200 K for two different distances down the diffusion tube (as indicated in the legend). The plotted values represent integrated photon counts for several selected lines, as indicated in Fig. 7. The signals have been absolutely calibrated using  $^{14}\text{N}^{16}\text{O}$  to obtain the corresponding number densities (see text).

The number density values obtained by  $^{14}\text{N}^{16}\text{O}$  calibration are in the  $10^{11} \text{ cm}^{-3}$  range, which is too high to be attributed to three-body  $\text{N} + \text{O}$  recombination at the low pressure and high temperature used in the experiment. Therefore, they have to be produced by surface-catalyzed processes. The background NO LIF signal is sizable at this high temperature, and its behavior as a function of the titration flow rate must be understood separately before it is subtracted from the total signal. This was made possible by the  $^{15}\text{N}^{18}\text{O}$  titration experiments.

Figure 9 shows spectra measured at 1200 K using  $^{15}\text{N}^{18}\text{O}$  titration. A different spectral region is selected than in the case of  $^{15}\text{N}^{16}\text{O}$  titration. The situation is also more complicated in this case, because both  $^{14}\text{N}^{16}\text{O}$  and  $^{14}\text{N}^{18}\text{O}$  features are observed in the spectrum for all titration flow rates below the endpoint. However,  $^{14}\text{N}^{16}\text{O}$  and  $^{15}\text{N}^{18}\text{O}$  spectra that we measured separately allow us to assign the observed  $^{14}\text{N}^{16}\text{O}$  transitions unambiguously and, by exclusion, those transitions that belong to neither  $^{14}\text{N}^{16}\text{O}$  nor  $^{15}\text{N}^{18}\text{O}$  are assigned to  $^{14}\text{N}^{18}\text{O}$ . The line assignments, as well as the lines used to trace the dependences of  $^{14}\text{N}^{16}\text{O}$  and  $^{14}\text{N}^{18}\text{O}$  number densities on the titration flow rate are marked in Figure 9. The bottom panel in Figure 9 shows the spectrum measured above the endpoint, showing only the strong lines of the  $^{15}\text{N}^{18}\text{O}$  titration agent.

Figure 10 shows the dependences of the  $^{14}\text{N}^{16}\text{O}$  and  $^{14}\text{N}^{18}\text{O}$  number densities on the  $^{15}\text{N}^{18}\text{O}$  titration flow rate. The signals from the two PMTs have been cross-calibrated, as described above. The  $^{14}\text{N}^{16}\text{O}$  background signal decreases with the flow rate in an approximately linear fashion, and a linear fit to this dependence would yield a non-zero value at the titration endpoint. Near the endpoint the  $^{14}\text{N}^{16}\text{O}$  signal abruptly drops to zero. The decrease in the background  $^{14}\text{N}^{16}\text{O}$  signal with increasing titration flow is not surprising, given that no new  $^{16}\text{O}$  atoms are added in the system, whereas the number density of  $^{14}\text{N}$  atoms decreases with the addition of  $^{15}\text{N}^{18}\text{O}$  titration flow. The strong deviation from linear dependence near the endpoint and the abrupt drop to zero are harder to

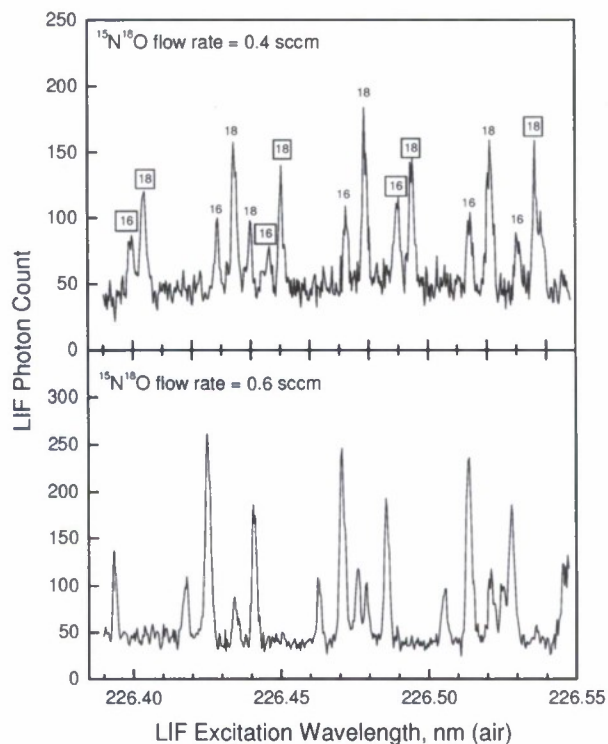


Figure 9. LIF spectra at 1200 K obtained using  $^{15}\text{N}^{18}\text{O}$  titration. The spectra were measured at a distance of 100 cm down the diffusion tube and represent the sum photon count for 20 laser pulses. Top: spectrum measured below the titration endpoint, showing lines of  $^{14}\text{N}^{18}\text{O}$  (labeled by '18') and  $^{14}\text{N}^{16}\text{O}$  (labeled by '16'). The lines that were used to calculate the changes of LIF intensities with the titration flow rate (Fig. 10) have labels enclosed in squares. Bottom: spectrum measured above the titration endpoint, showing only  $^{15}\text{N}^{18}\text{O}$  lines.

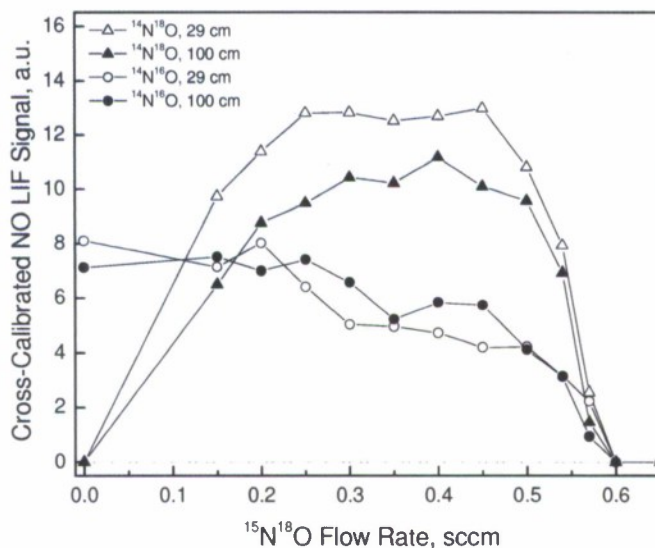


Figure 10. LIF signal intensities for  $^{14}\text{N}^{18}\text{O}$  and  $^{14}\text{N}^{16}\text{O}$  as functions of the  $^{15}\text{N}^{18}\text{O}$  titration flow rate. Measurements were performed at 1200 K for two different distances down the diffusion tube (as indicated in the legend). The plotted values represent integrated photon counts for several selected lines, as indicated in Fig. 9. The signals have been normalized with respect to the excitation pulse energy and cross-calibrated with respect to the PMT detection sensitivities (see text).

understand without a detailed model. However, we note that the probed steady-state  $^{14}\text{N}^{16}\text{O}$  number density is determined by a competition between the surface-catalyzed production and collisional removal by N atoms; rates for both processes increase with the N-atom number density, and in such a situation strong nonlinearities near zero N-atom number density (endpoint) are not surprising.

The  $^{14}\text{N}^{18}\text{O}$  signal plotted in Figure 10 is zero at zero titration flow, and it increases with flow rate with a noticeable curvature. Similar to the data in Figure 8, the curve exhibits a rather broad peak near 2/3 of the endpoint flow rate, and then rather abruptly decreases to zero. The  $^{14}\text{N}^{16}\text{O}$  data in Fig. 8, which include the flow rate-dependent background signal contribution, show no significant curvature below 0.4 sccm, but we note that the experimental uncertainty is significant enough that such curvature cannot be excluded. The general shape of the  $^{14}\text{N}^{18}\text{O}$  signal dependences plotted in Figure 10 provides key guidance for our surface chemistry model. The fact that the  $^{14}\text{N}^{18}\text{O}$  signal is purely titration induced, i.e., it disappears at both zero titration flow and titration endpoint, unambiguously proves that  $^{14}\text{N}^{18}\text{O}$  is a result of a reaction between  $^{18}\text{O}$  atoms introduced by titration and  $^{14}\text{N}$  atoms produced by  $\text{N}_2$  dissociation in the discharge.

For the purpose of initial analysis, we assume that the total NO number density, such as data plotted in Fig. 8, is a simple sum of the background and titration-induced number densities for any titration flow rate. We can then extract the titration-induced number density using  $^{15}\text{N}^{18}\text{O}$  titration data as guidance. At zero titration flow, all of the NO number density plotted in Fig. 8 is a result of the background production. At, e.g., 0.4 sccm titration flow rate, Fig. 10 indicates that this initial background number density is reduced by about 50% for a distance of 29 cm down the tube. Thus, from the total NO signal at 0.4 sccm we subtract 50% of the initial (zero-flow) signal to obtain the titration-induced number density. Such analysis was done for all investigated temperatures and the results are plotted in Fig. 11.

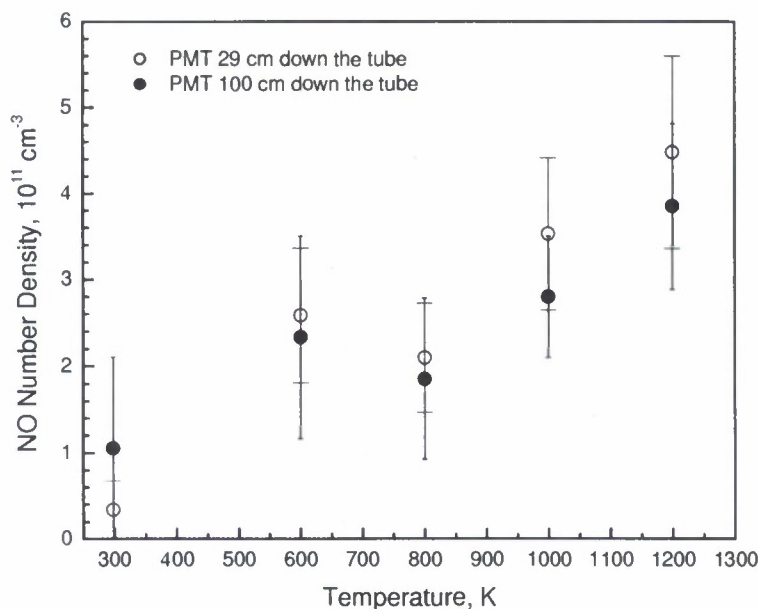


Figure 11. Number density of surface-produced  $^{14}\text{N}^{16}\text{O}$  as a function of temperature for two positions down the diffusion tube. The data was obtained using  $^{15}\text{N}^{16}\text{O}$  titration, with a titration flow rate corresponding to 70% of the endpoint. The background signal was subtracted to obtain the  $^{14}\text{N}^{16}\text{O}$  density due solely to the O atoms introduced by titration (see text).

The room-temperature NO signals are very small and the error bars in Fig. 11 hence include zero; the method is not well suited for low temperatures and it is thus complementary to the O- and N-atom detection approach described in the previous section. The NO density exhibits a relatively rapid increase with temperature, except for the possible drop between 600 and 800 K.

Because of the experimental complexity of these experiments, sufficient time did not remain to complete finite-rate surface chemistry modeling of these results. However, the same model used in the previous set of experiments shows qualitative agreement with the measured behavior of the surface generated NO.

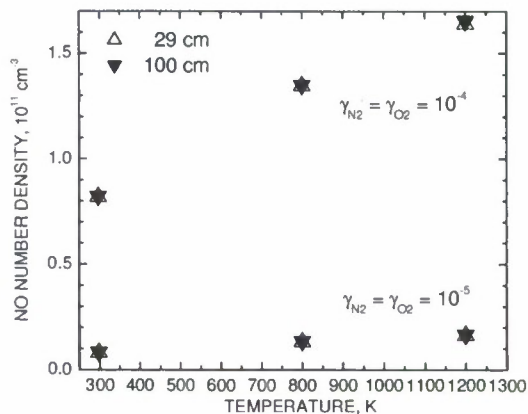
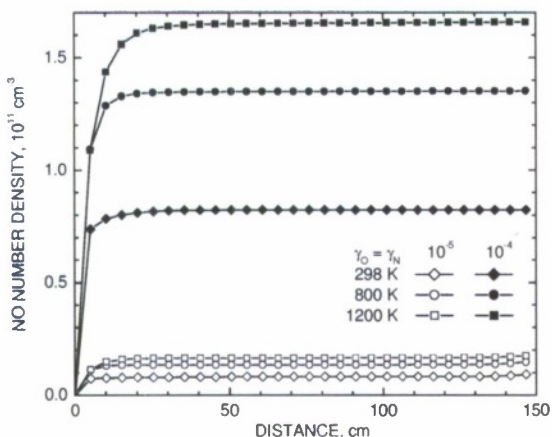
**Table 4 Gas-phase reactions with temperature dependence**

|     | Reaction                          | Rate <sup>a</sup>                                     | References |
|-----|-----------------------------------|---|------------|
| R1  | $O + O + M \rightarrow O_2 + M$   | $k_1 = 1.57 \times 10^{-34} T^0 \exp(900/T)$          | 38         |
| R2  | $O + O_2 + M \rightarrow O_3 + M$ | $k_2 = 3.9 \times 10^{-29} T^{-2} \exp(-140/T)$       |            |
| R2b | $O_3 + M \rightarrow O + O_2 + M$ | $k_{2b} = 4.13 \times 10^{-10} T^{-0} \exp(-11430/T)$ | 38         |
| R3  | $O + O_3 \rightarrow O_2 + O_2$   | $k_3 = 8.6 \times 10^{-12} T^0 \exp(-2090/T)$         | 38         |
| R4  | $O + N + M \rightarrow NO + M$    | $k_4 = 1.8 \times 10^{-31} T^{-0.5} \exp(0/T)$        | 21         |
| R5  | $O + NO + M \rightarrow NO_2 + M$ | $k_5 = 4.2 \times 10^{-33} T^0 \exp(940/T)$           | 21         |
| R6  | $O + NO_2 \rightarrow NO + O_2$   | $k_6 = 1.7 \times 10^{-11} T^0 \exp(-300/T)$          | 21         |
| R7  | $N + N + M \rightarrow N_2 + M$   | $k_7 = 8.3 \times 10^{-34} T^0 \exp(500/T)$           | 21         |
| R8  | $N + NO \rightarrow N_2 + O$      | $k_8 = 2.7 \times 10^{-11} T^0 \exp(0/T)$             | 21         |
| R9  | $N + NO_2 \rightarrow N_2O + O$   | $k_9 = 5.8 \times 10^{-12} T^0 \exp(220/T)$           | 20         |

<sup>a</sup> Bimolecular rate constants are in units of  $\text{cm}^3 \text{ molecule}^{-1} \text{ s}^{-1}$ . Termolecular rate constants are in units of  $\text{cm}^6 \text{ molecule}^{-2} \text{ s}^{-1}$ , and the collision partner M is taken as  $\text{N}_2$ .

The temperature-dependent gas-phase reaction rates of Table 4 were used for these calculations. The general form for these reaction rates is taken as  $k_1 = AT^n \exp(-(E/R)/T)$ , with specified constants  $A$ ,  $n$ , and  $E/R$ , which can sometimes be zero. Because ozone thermally dissociates at appreciable rates above  $\sim 500$  K, one more equation (R2b) was added to the gas-phase reaction set.

In the simulations shown below, the entire diffusion tube is modeled as isothermal, the total pressure is 58.5 Pa, titration endpoint is 0.6 sccm in a 73 sccm  $\text{N}_2$  flow, and the branching fractions are specified as  $f_{N,N_2} = f_{O,O_2} = 0.5$ .



a)

b)

**Figure 12.** a) Number density of surface-produced NO as a function of distance from the side-arm entrance for three different temperatures and two different reaction efficiencies; b) number density 29 cm and 100 cm from the side-arm entrance as a function of temperature for two different reaction efficiencies. The dissociated nitrogen flow was 2/3 titrated.

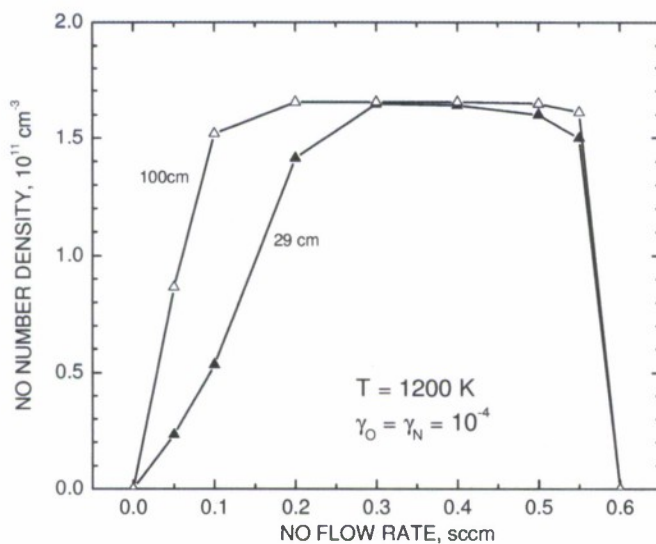


**Figure 13.** Number density of surface-produced NO as a function of NO added at the titration port, at distances of 29 cm and 100 cm from the side-arm entrance.

Figures 12a and 12b show the model predictions for NO number density as a function to temperature, distance from the side-arm entrance and reaction efficiency. The NO number density rises with increasing temperature and increasing reaction efficiency, and is relatively constant along the side-arm tube beyond ~20 cm from the tube entrance.

The predicted NO number densities are on the order of  $10^{11} \text{ cm}^{-3}$  for a reaction efficiency of  $10^{-4}$ , in excellent agreement with experiment, considering the many reaction and diffusion parameters that must be input into the program. We note that computations made with or without reaction R4 over our entire temperature range produce essentially identical numerical results, so the gas-phase production of NO by O + N recombination is negligible compared to the surface production of NO, as stated earlier.

The rise of NO number density observed experimentally (Fig. 11) is about a factor of four from 298 to 1200 K, while it is only about a factor of two over this temperature range in model predictions for fixed reaction efficiency (Fig. 12b). However, the reaction efficiency for atom loss on quartz is expected to increase with temperature, so the agreement between computations and experiment could easily be improved by adjusting the input reaction efficiency as a function of temperature.

Figure 13 shows the predicted variation of the surface-produced NO, 29 cm and 100 cm from the side-arm entrance, as a function of NO added at the titration point. The calculations are for a temperature of 1200 K assuming a reaction efficiency of  $10^{-4}$ . Figure 13 can be compared to the experimental  $^{14}\text{N}^{18}\text{O}$  data of Fig. 10. The computations do a good job of reproducing the asymmetry of the NO number density variation with titration gas addition, rising more slowly with the introduction of NO and falling more rapidly near the titration end-point. The model predicts that NO concentrations at 100 cm should be equal to or greater than at 29 cm. Experimentally the number density is usually higher at 29 cm than at 100 cm (Fig. 10 and 11), but the error bars on the measured number densities are substantial and overlap (Fig. 11).

It was not possible to implement the non-isothermal tube wall temperature into the computations at this time, nor to do a sensitivity study on the gas-phase reaction coefficients, in particular reaction R8. However, both will be performed and the conclusions will be included in a manuscript currently under preparation describing these experiments.

## SUMMARY

During this project we have conclusively demonstrated the importance of the O + N surface reaction for catalytic atom recombination processes on silica surfaces in dissociated nitrogen-oxygen mixtures. This was accomplished using a diffusion tube side-arm reactor, a microwave discharge to generate atomic nitrogen, and an NO titration technique to generate different mixtures of O and N atoms, together with two distinct species diagnostic approaches.

In the first approach, two-photon LIF of atomic oxygen and atomic nitrogen were used to show how the relative atom concentrations varied with position along the diffusion tube as a function of O/N ratio at the diffusion tube inlet. The experimental result confirmed and extended earlier experiments by Copeland et al.<sup>11</sup> and were consistent with a reaction-diffusion model of the diffusion tube in which O + N surface reaction plays a comparable role to O + O and N + N.

In the second approach, single-photon LIF was used together with isotopically-labeled titration gases to detect surface-produced NO directly at two different positions in the diffusion tube, as a function of O/N ratio at the diffusion tube inlet. These experiments independently confirm the production of NO by surface reactions on quartz, from room temperature up to 1200 K. The same reaction-diffusion model used to interpret the previous room-temperature experiments can also reproduce most features of the new experimental data at higher temperatures.

## REFERENCES

- <sup>1</sup>Pejaković, D., Marschall, J., Duan, L., and Martin, M.P., "Nitric Oxide Production from Surface Recombination of Oxygen and Nitrogen Atoms," AIAA 2008-1249, January 2008.
- <sup>2</sup>Pejaković, D., Marschall, J., Duan, L., and Martin, M.P., "Nitric Oxide Production from Surface Recombination of Oxygen and Nitrogen Atoms," *Journal of Thermophysics and Heat Transfer*, Vol. 22, No. 2, 2008, pp. 178-186.
- <sup>3</sup>Natsui, F., Barbato, M., and Bruno, C., "Material-Dependent Catalytic Recombination Modeling for Hypersonic Flows," *Journal of Thermophysics and Heat Transfer*, Vol. 10, No. 1, 1996, pp. 131-136.
- <sup>4</sup>Daiß, A., Frühauf, H.-H., and Messerschmid, E.W., "Modeling of Catalytic Reactions on Silica Surfaces with Consideration of Slip Effects," *Journal of Thermophysics and Heat Transfer*, Vol. 11, No. 3, 1997, pp. 346-352.
- <sup>5</sup>Deutschmann, O., Riedel, U., and Warnatz, J., "Modeling of Nitrogen and Oxygen Recombination on Partial Catalytic Surfaces," *Journal of Heat Transfer*, Vol. 117, No. May, 1995, pp. 495-501.
- <sup>6</sup>Kovalev, V.L., Suslov, O.N., and Triskiy, G.A., "Phenomenological Theory for Heterogeneous Recombination of Partially Dissociated Air on High-Temperature Surfaces," in *Molecular Physics and Hypersonic Flows*, edited by M. Capitelli, (Kluwer Academic, Boston, 1996), p. 193-202.
- <sup>7</sup>Kurotaki, T., "Catalytic Model on SiO<sub>2</sub>-Based Surface and Application to Real Trajectory," *Journal of Spacecraft and Rockets*, Vol. 38, No. 5, 2001, pp. 798-800.
- <sup>8</sup>Armenise, I., Barbato, M., Capitelli, M., and Kustova, E., "State-to-State Catalytic Models, Kinetics, and Transport in Hypersonic Boundary Layers," *Journal of Thermophysics and Heat Transfer*, Vol. 20, No. 3, 2006, pp. 465-476.
- <sup>9</sup>Daiß, A., Frühauf, H.-H., and Messerschmid, E.W., "Chemical Reactions and Thermal Nonequilibrium on Silica Surfaces," in *Molecular Physics and Hypersonic Flows*, edited by M. Capitelli, (Kluwer Academic, Boston, 1996), p. 203-218.
- <sup>10</sup>Laux, T., Feigl, M., Stöckle, T., and Auweter-Kurtz, M., "Estimation of the Surface Catalyticity of PVD-Coatings by Simultaneous Heat Flux and LIF Measurements in High Enthalpy Air Flows," AIAA Paper 2000-2364, June 2000.
- <sup>11</sup>Copeland, R.A., Pallix, J.B., and Stewart, D.A., "Surface-Catalyzed Production of NO from Recombination of N and O Atoms," *Journal of Thermophysics and Heat Transfer*, Vol. 12, No. 4, 1998, pp. 496-499.
- <sup>12</sup>Smith, W.V., "The Surface Recombination of H Atoms and OH Radicals," *Journal of Chemical Physics*, Vol. 11, No. March, 1943, pp. 110-125.
- <sup>13</sup>Wise, H. and Wood, B.J., "Reactive Collisions Between Gas and Surface Atoms," in *Advances in Atomic and Molecular Physics*; Vol. 3, edited by D. R. Bates and I. Estermann, (Academic Press, New York, 1967), p. 291-353.
- <sup>14</sup>Pallix, J.B. and Copeland, R.A., "Measurement of Catalytic Recombination Coefficients on Quartz Using Laser-Induced Fluorescence," *Journal of Thermophysics and Heat Transfer*, Vol. 10, No. 2, 1996, pp. 224-233.
- <sup>15</sup>Kim, Y.C. and Boudart, M., "Recombination of O, N, and H Atoms on Silica: Kinetics and Mechanism," *Langmuir*, Vol. 7, No. 12, 1991, pp. 2999-3005.
- <sup>16</sup>Marschall, J., "Experimental Determination of Oxygen and Nitrogen Recombination Coefficients at Elevated Temperature Using Laser-Induced Fluorescence," AIAA Paper 97-3879, August 1997.

- <sup>17</sup>Marschall, J., Chamberlain, A., Crunkleton, D., and Rogers, B., "Catalytic Atom Recombination on ZrB<sub>2</sub>/SiC and HfB<sub>2</sub>/SiC Ultrahigh-Temperature Ceramic Composites," *Journal of Spacecraft and Rockets*, Vol. 41, No. 4, 2004, pp. 576-581.
- <sup>18</sup>Marschall, J., Copeland, R.A., Hwang, H.H., and Wright, M.J., "Surface Catalysis Experiments on Metal Surfaces in Oxygen and Carbon Monoxide Mixtures," AIAA Paper 2006-181, January 2006.
- <sup>19</sup>Sepka, S., Chen, Y.-K., Marschall, J., and Copeland, R.A., "Experimental Investigation of Surface Reactions in Carbon Monoxide and Oxygen Mixtures," *Journal of Thermophysics and Heat Transfer*, Vol. 14, No. 1, 2000, pp. 45-52.
- <sup>20</sup>Sander, S.P., Friedl, R.R., Golden, D.M., Kurylo, M.J., Moortgat, G.K., Wine, P.H., Ravishankara, A.R., Kolb, C.E., Molina, M.J., Finlayson-Pitts, B.J., Huie, R.E., and Orkin, V.L., "Chemical Kinetics and Photochemical Data for Use in Atmospheric Studies: Evaluation Number 15," JPL Publication 06-2, NASA, July 10, 2006.
- <sup>21</sup>Baulch, D.L., Drysdale, D.D., and Horne, D.G., *Evaluated Kinetic Data for High Temperature Reactions, Volume 2: Homogeneous Gas Phase Reactions of the H<sub>2</sub>-N<sub>2</sub>-O<sub>2</sub> System*, Butterworths, London, 1973.
- <sup>22</sup>Bischel, W.K., Perry, B.E., and Crosley, D.R., "Detection of Fluorescence from O and N Atoms Induced by Two-Photon Absorption," *Applied Optics*, Vol. 21, No. 8, 1982, pp. 1419-1429.
- <sup>23</sup>Bischel, W.K., Perry, B.E., and Crosley, D.R., "Two-Photon Laser-Induced Fluorescence in Oxygen and Nitrogen Atoms," *Chemical Physics Letters*, Vol. 82, No. 1, 1981, pp. 85-88.
- <sup>24</sup>Adams, S.F. and Miller, T.A., "Two-Photon Absorption Laser Induced Fluorescence of Atomic Nitrogen by an Alternative Excitation Scheme," *Chemical Physics Letters*, Vol. 295, No. 4, 1998, pp. 305-311.
- <sup>25</sup>Repsilber, T. and Uhlenbusch, J., "Absolute Calibration of TALIF of Atomic Nitrogen by NO Titration - Experimental and Theoretical Analysis," *Plasma Chemistry and Plasma Processing*, Vol. 24, No. 3, 2004, pp. 373-392.
- <sup>26</sup>Von Weysenhoff, H. and Patapoff, M., "Validity and Limitations of the Gas Titration of Atomic Nitrogen with Nitric Oxide," *Journal of Physical Chemistry*, Vol. 69, No. 5, 1965, pp. 1756-1758.
- <sup>27</sup>Young, R.A., Sharpless, R.L., and Stringham, R., "Catalyzed Dissociation of N<sub>2</sub> in Microwave Discharges. I," *Journal of Chemical Physics*, Vol. 40, No. 1, 1964, pp. 117-119.
- <sup>28</sup>Arasa, C., Gamallo, P., and Sayós, R., "Adsorption of Atomic Oxygen and Nitrogen at  $\beta$ -Crisobalite (100): A Density Functional Theory Study," *Journal of Physical Chemistry B*, Vol. 109, No. 31, 2005, pp. 14954-14964.
- <sup>29</sup>Cozmuta, I., "Molecular Mechanisms of Gas Surface Interactions in Hypersonic Flow," AIAA Paper 2007-4046, June 2007.
- <sup>30</sup>Schlichting, H., *Boundary-Layer Theory*, McGraw-Hill, New York, 1979.
- <sup>31</sup>Touloukian, Y.S., Saxena, S.C., and Hestermans, P., *Thermophysical Properties of Matter. Viscosity*, Vol. 11 IFI/Plenum, New York, 1975.
- <sup>32</sup>Ramshaw, J.D., "Self-Consistent Effective Binary Diffusion in Multicomponent Gas Mixtures," *Journal of Non-Equilibrium Thermodynamics*, Vol. 15, No. 3, 1990, pp. 295-300.
- <sup>33</sup>Ramshaw, J.D. and Chang, C.H., "Friction-Weighted Self-Consistent Effective Binary Diffusion Approximation," *Journal of Non-Equilibrium Thermodynamics*, Vol. 21, No. 3, 1996, pp. 223-232.
- <sup>34</sup>Wright, M.J., Bose, D., Palmer, G.E., and Levine, E., "Recommended Collision Integrals for Transport Property Computations, Part 1: Air Species," *AIAA Journal*, Vol. 43, No. 12, 2005, pp. 2558-2564.

<sup>35</sup>Wright, M.J., Hwang, H.H., and Schwenke, D.W., "Recommended Collision Integrals for Transport Property Computations Part 2: Mars and Venus Entries," *AIAA Journal*, Vol. 45, No. 1, 2007, pp. 281-288.

<sup>36</sup>Gupta, R., Yos, J., Thompson, R., and Lee, K., "A Review of Reaction Rates and Thermodynamic and Transport Properties for an 11-Species Air Model for Chemical and Thermal Nonequilibrium Calculations to 30000 K," NASA RP-1232, NASA, August 1990.

<sup>37</sup>Wright, M.J., Candler, G.V., and Bose, D., "Data-Parallel Line Relaxation Method for the Navier-Stokes Equations," *AIAA Journal*, Vol. 36, No. 9, 1998, pp. 1603-1609.

<sup>38</sup>Baulch, D.L., Drysdale, D.D., Duxbury, J., and Grant, S.J., *Evaluated Kinetic Data for High Temperature Reactions, Volume 3. Homogeneous Gas Phase Reactions of the O<sub>2</sub>-O<sub>3</sub> system, the CO-O<sub>2</sub>-H<sub>2</sub> system, and of Sulfur-Containing Species.*, Butterworths, London, 1976.

<sup>39</sup>Bose, D. and Wright, M., "Uncertainty Analysis of Laminar Aeroheating Predictions for Mars Entries," AIAA Paper 2005-4682, June 2005.

<sup>40</sup>Back, R.A. and Mui, J.Y.P., "The Reactions of Active Nitrogen with N<sup>15</sup>O and N<sub>2</sub><sup>15</sup>," *Journal of Physical Chemistry*, Vol. 66, No. 7, 1962, pp. 1362-1364.

<sup>41</sup>Wang, D., Stallcop, J.R., Huo, W.M., Dateo, C.E., Schwenke, D.W., and Partridge, H., "Quantal Study of the Exchange Reaction for N+N<sub>2</sub> Using an *ab initio* Potential Energy Surface," *Journal of Chemical Physics*, Vol. 118, No. 5, 2003, pp. 2186-2189.

<sup>42</sup>Garcia, E., Saracibar, A., Laganà, A., and Skouteris, D., "The Shape of the Potential Energy Surface and the Thermal Rate Coefficients of the N + N<sub>2</sub> Reaction," *Journal of Physical Chemistry A*, Vol. 111, No. 41, 2007, pp. 10362-10368.

<sup>43</sup>Gordiets, B.F., Ferreira, C.M., Guerra, V.L., Loureiro, J.M., Nahorny, J., Pagnon, D., and Vialle, M., "Kinetic Model of a Low-Pressure N<sub>2</sub>-O<sub>2</sub> Flowing Glow Discharge," *IEEE Transactions On Plasma Science*, Vol. 23, No. 4, 1995, pp. 750-768.

<sup>44</sup>Guerra, V., Sá, P.A., and Loureiro, J., "Role Played by the N<sub>2</sub>(A <sup>3</sup>Σ<sub>u</sub><sup>+</sup>) Metastable in Stationary N<sub>2</sub> and N<sub>2</sub>-O<sub>2</sub> Discharges," *Journal of Physics D: Applied Physics*, Vol. 34, 2001, pp. 1745-1755.